Hugoniot elastic limit of single-crystal tantalum at normal and elevated temperatures subjected to extreme strain rates

Anuradha Singla [1,*] and Aditi Ray [1,2]
[1]*Theoretical Physics Section, Bhabha Atomic Research Centre, Mumbai - 400085, India*
[2]*Homi Bhabha National Institute, Mumbai - 400094, India*

(Received 15 July 2021; revised 21 January 2022; accepted 24 January 2022; published 11 February 2022)

Large-scale nonequilibrium molecular dynamic simulations of impact-induced shock propagation in defect-free single-crystal Ta along the [001] direction is presented, paying particular attention to the formation of elastic-plastic two-wave structures. Plastic deformation and elastic limits of Ta single crystals for various crystal orientations were investigated in a recent paper [R. Ravelo *et al.*, Phys. Rev. B **88**, 134101 (2013)]. In the present paper, a comprehensive study on the Hugoniot elastic limit (HEL) and its dependence on associated physical parameters is reported. The observed attenuation of an elastic precursor in a stress-wave profile led to proposing wide-range scaling relations for HEL decay applicable for ultrahigh strain rates. The influence of a lateral dimension on the spatial profile of a stress wave and time profile of free surface velocity (FSV) in the distinct appearance of a spike-valley feature and its consequence on scaling relations is investigated. Further, it is shown that the commonly used method of calculating HEL from a FSV profile is inadequate for submicron-thick samples at high strain rates. The necessary modifications are incorporated that resulted in comparable HEL values by two complimentary approaches of stress and FSV profiles. Simulations carried out for increasing impact strength revealed a power law dependence of HEL with strain rate. A methodology based on extrapolation of stress decay law and strain rate scaling constructed by us is proposed here for prediction of HEL pertaining to larger length samples. Very good agreement between the predicted values and available experimental results makes the modeling robust and applicable for a wide range of strain rates and length scales. Finally, the study is extended for elevated sample temperatures up to melting. Interestingly, yield strength is shown to follow an increasing trend up to a certain temperature, beyond which it decreases. An empirical relation is proposed here for expressing temperature dependence of HEL that explains the observed yield strength anomaly. Results are justified through thermal analysis of shear stress and evolution of dislocation density.

DOI: 10.1103/PhysRevB.105.064102

I. INTRODUCTION

In high energy density systems [1], such as impact-driven phenomena, hypervelocity launch, laser and high explosive-driven shocks, equation of state studies, and inertial confinement fusion, materials experience large volumetric changes along with a wide range of microstructural evolution. It is necessary to investigate material behavior in terms of its strength and integrity under extreme dynamic compression. Shock-induced dynamic compression of crystalline solids has been extensively studied in the past [2–7].

An elastic-plastic (EP) model of mechanical response provides sufficient insight into the resistance of a material to shock-induced structural changes that includes defect formation, dislocations nucleation, and growth and plastic deformation. All these phenomena lead to stress relaxation and subsequent attenuation of elastic precursors, quantitatively expressed in terms of dynamic yield strength or Hugoniot elastic limit (HEL) of the material. It is defined as the elastic stress value for which material starts exhibiting plastic properties.

Mechanism of shock propagation in fcc metals has been well studied experimentally as well as through simulations [8,9]. But the same does not hold true for BCC metals due to the inherent complexities involved. Dynamic yield strength of many BCC metals, which is of interest in the current paper, has been investigated experimentally [10–13]. Among BCC metals, Ta and Ta-based alloys have several technological advantages and are widely used in many high-pressure applications. This is due to their excellent mechanical properties, such as high strength, hardness, and temperature resistance, along with its high density and high melting temperature. While thermodynamic properties of shock-loaded Ta at ultrahigh strain rates have been studied to a good extent [14,15], there exists a strong need to assess its macroscopic mechanical properties, such as yield strength, work-hardening, fracture toughness, etc.

Most studies in unravelling response under high dynamic compression and determination of yield strength of Ta are limited to strain rates ranging from 10^{-3} to 10^{-1} s^{-1} (quasistatic) and in the intermediate range of 10^{3} to 10^{5} s^{-1} [16,17]. With currently available experimental techniques, such as two-stage light gas gun and lasers, the study of EP yielding of crystalline structures has been extended to moderately high strain rates. There are reports of experimental determination of HEL of mm-sized single and polycrystalline Ta [12,18–23] as well as Ta-based alloys [24] for strain rate lying in the range of $10^{5} - 10^{7}$ s^{-1}. In a higher strain-rate regime (10^{9} s^{-1}),

*Corresponding author: anuradhas@barc.gov.in

dynamic yielding of submicron to few micron thick Ta samples are examined by use of ultrashort laser pulses [25–27].

Dynamics of shock waves in different materials have been studied numerically through the evolution of mobile and immobile dislocations [28]. The approach successfully reproduces experimentally observed distance and target temperature variations of elastic precursors. Recently, application of dislocation-based plasticity models in continuum mechanics has been used by Khishchenko and Mayer [29] to determine the structure of EP waves. Theoretical modeling of elastic precursor decay in shock-loaded Ta supported by dislocations analysis are reported by many authors [9,18,30–32].

Nonetheless, existing technologies are not well suited for experimental exploration of plastic deformation of mm-size samples at still higher strain rates. At these regimes, the timescale of the shock-induced deformation process is too short (ps to fs) to be accurately probed in any experiment. It is for this purpose that a molecular dynamics (MD) study that facilitates extracting information about shock evolution and associated microstructural changes at such exotic environment is employed [33].

Due to steady growth in computational capabilities and development of accurate interatomic potentials, the last decade has seen significant advancement in MD-based studies of dynamic compression phenomena, leading to determination of material strength. It has also revealed plastic deformation mechanisms, like dislocation nucleation and growth, twinning and spall, phase transitions, etc. in bcc [34–37] and fcc [38–40] as well as other materials [41–43]. MD simulations of Ravelo *et al.* [44] on shock-induced plasticity provided information about elastic-plastic two-wave (EPTW) regions of Ta single crystal.

While experiments as well as MD simulation studies for most of the fcc [13,45–49] and hcp [50,51] metals show a consistent increase of HEL with temperature for strain rates varying within $10^3 - 10^7$ s^{-1}, the same for BCC metals is inconclusive [10,13,19,52].

The temperature and strain-rate dependence of the flow stress of Ta has been studied between 78 K to 800 K at varied strain rates of 10^{-5} to 10^4 s^{-1} [53]. HEL of mm-thick Ta samples has been determined experimentally [19] at 300 K, 800 K, and 1300 K. However, no systematic trend for temperature dependence on HEL was reported. Experiments conducted for higher sample temperatures up to 2600 K revealed a decreasing trend of HEL [54,55], thereby validating the Zerilli-Armstrong model [56] for bcc Ta. These studies belonging to polycrystalline samples are restricted to a strain rate less than 10^3 s^{-1}. To the best of our knowledge, a temperature-induced study on EP response of single crystal Ta at extreme strain rates has not been examined yet.

The aim of the present paper is to investigate formation of EPTW regions and subsequent advancement of elastic precursors within single-crystal Ta samples through extensive MD simulation of impact-induced shock propagation. Microscopically tracking EP transitions perceived well-formed decay patterns of the elastic stress amplitude with wave propagation. Distinct empirical scaling relations for elastic stress decay associated with spike and valley positions are constructed. This study enabled determination of spike-valley based HEL for two different submicron-sized samples.

In an attempt to understand the mechanism of elastic precursor decay, the influence of various physical parameters pertaining to samples like length, lateral dimension, and initial temperature on HEL are investigated as a function of increasing impact strength. A generalized power-law scaling relation is proposed for expressing strain-rate dependence of HEL.

Most importantly, it is shown that the HEL of a mm-size sample predicted by extrapolating the proposed decay law constructed based on results of submicron-length samples, along with the strain-rate scaling relation we developed, is in excellent agreement with experimental results. Thus the separation of the variable approach adopted in this paper successfully bridges the gap of length scales (submicron to millimeter) and strain rates ($10^4 - 10^{10}$ s^{-1}). This would save the requirement of exhaustive computational resources for simulation of larger length samples.

Further, the influence of elevated sample temperatures on EPTW transition, appearance of spike-valley separation in elastic precursors, and, finally, HEL of Ta single crystals has been investigated. Our paper demonstrates that HEL initially increases with temperature, reaches maximum at certain characteristic values depending on loading stress, and then follows a gradual decrease due to thermal activation. An empirical law for explaining temperature dependence of HEL, incorporating the observed yield strength anomaly (YSA), is proposed here. The striking results of thermal hardening of Ta is supported by extensive simulation and analysis of dislocation dynamics.

This paper is a comprehensive theoretical study on HEL of Ta at normal and elevated temperatures up to melting. This also solves, to a good extent, the need for developing a general theory of dynamic strength that can be extended from the atomistic scale to the bulk regime.

The organization of the paper is as follows. In Sec. II, we briefly discuss MD simulation essentials. Characteristic signatures of EP response in a spatial profile of a stress wave, determination of room-temperature HEL from the stress-wave profile, and influence of system dimensions on HEL decay are presented in Sec. III. Analysis of HEL estimated from the time profile of free surface velocity (FSV) is described in Sec. IV. The effect of increasing strain rate on HEL is modeled in Sec. V. Comparative analysis of our simulations results with experimental data are presented in Sec. VI. Section VII discusses the thermal influence of EP behavior and attenuation of yield strength for increasing impact strength. Important conclusions are summarized in Sec. VIII.

II. MD SIMULATION METHODOLOGY

The present study of shock propagation in single-crystal Ta has been carried out by large-scale NEMD simulations using an open source MD code, LAMMPS [57].

We have used the recently developed embedded atom method based interatomic potential, referred to as Ta1 [44].

A. Simulation setup

In the current paper, we have considered a simulation box of dimensions N_x, N_y, and N_z number of unit cells (uc) along x,

y, and z axes. The effect of shock propagation has been studied for $N_z = 500$ and 2000 uc, corresponding to two different length samples of 165-nm and 660-nm, respectively. The lateral dimensions of the simulation box L_x $(=L_y)$ is varied from 6 nm ($N_x = 20$ uc) to 33 nm ($N_x = 100$ uc). The simulated Ta system thus contains 0.4 million to 40 million atoms. The direction of shock propagation has been aligned with the z axis.

Periodic boundary conditions are applied in x and y directions so particles can interact through xz and yz surfaces of the orthogonal simulation system. The shock direction (z) is maintained with a shrink-wrapped condition, thereby adjusting the box size to contain the same initial number of atoms wherever they move to. This condition sets the position of the free surface in the z direction so as to encompass all atoms [57]. The time step chosen for integration of the equation of motion is 1 fs. The system is first equilibrated at predefined sample temperature for 100 ps under NPT ensemble. For creating 1D shock-induced strain along the z direction, the first four unit cells (≈13 Å) on one end of the sample is set as an infinite-mass piston to drive the motion. Generation of shock is accomplished by giving atoms belonging to the piston a constant inward velocity (along the positive z direction) into the material. Piston velocity is tuned so as to capture EPTW coupled structure for the chosen crystal orientation. The impact-induced changes in crystal structure continue to propagate toward the far side of the simulation box and finally is reflected from the free surface as a rarefaction wave. The scenario is reminiscent of gas guns or explosive driven flyer plate impact, however, without explicit simulation of the flyer.

Spatial and temporal characteristics of shock-wave propagation have been facilitated by introducing a quasi-one-dimensional bin of width 10 Å along the loading direction (z) and maintaining the size along lateral directions (x,y)—same as the simulation box. The thermodynamic variables like stress, density, particle velocity, and temperature are obtained by averaging the contribution of atoms in each bin.

B. Calculation of physical variables

The stress has been calculated using the virial definition [58] given below:

$$\sigma_{\alpha\beta}(i) = -\frac{1}{V_i}\left[m_i v_i^{\alpha} v_i^{\beta} + \frac{1}{2}\sum_j F_{ij}^{\alpha} r_{ij}^{\beta}\right], \tag{1}$$

where V_i, m_i, and v_i are the atomic volume, mass, and velocity of atom i, respectively, and F_{ij} represents the force on atom i due to atom j. α and β represent the Cartesian coordinates. The first term gives a measure of thermal kinetic energy in which the binned center-of-mass translational velocity has been appropriately subtracted as highlighted in Ref. [59]. The second term of Eq. (1) provides a measure of stresses arising due to pairwise interaction. Total pressure P is calculated as

$$P = -\tfrac{1}{3}[\sigma_{xx} + \sigma_{yy} + \sigma_{zz}], \tag{2}$$

where σ_{xx}, σ_{yy}, and σ_{zz} are the stresses averaged over the entire system in x, y, and z directions, respectively.

The shear stress, τ, is calculated as

$$\tau = \tfrac{1}{2}\left[\sigma_{zz} - \tfrac{1}{2}(\sigma_{xx} + \sigma_{yy})\right] = \tfrac{3}{4}[\sigma_{zz} - \sigma], \tag{3}$$

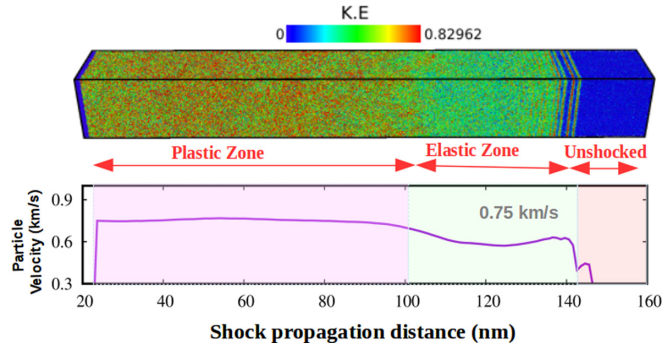

FIG. 1. Illustration of EPTW propagation within 165-nm-thin Ta sample when impacted at 0.75 km/s. Shock propagation direction coincides with [001] crystal direction. Top frame shows atoms colored according to their kinetic energies, with red being maximum and blue corresponding to zero velocity (undisturbed). Bottom panel shows the snapshot of spatial distribution of particle velocity at 32 ps.

where σ is the total stress in the system. For convenience, throughout this paper we shall be referring to absolute values of stresses.

Microstructural understanding and dislocation analysis of the shock-compressed sample is carried out using dislocation extraction algorithm (DXA) in visualization software OVITO [60].

III. ELASTIC-PLASTIC RESPONSE AT ROOM TEMPERATURE

Impact-induced shock of any strength causes both reversible and irreversible changes in the structure of a solid. Depending on the orientation in which crystal is loaded, impact velocity below a certain value generates a pure elastic wave, whereas impact strength exceeding a certain high value causes the pure plastic wave. For impact velocity, falling between the two extreme regimes leads to a coupled feature of elastic, EPTW, and plastic disturbances propagating through the target as illustrated in Fig. 1. The present paper is limited to shock applications along [001] direction.

Figures 2(a)–2(c) display the advancement of waves through 165-nm Ta single crystal for three different piston velocities. The solid curves show longitudinal stress σ_{zz} as a function of shock propagation distance for eight different time snapshots (starting from 4 ps to 32 ps with an increment of 4 ps), whereas dashed lines refer to shear stress, τ (doubled) at four alternate times. The impact at $U = 0.6$ km/s shown in Fig. 2(a) corresponds to the pure elastic wave. Our simulation revealed that the first appearance of the distinct two-wave structure occurs for impact at 0.75 km/s [Fig. 2(b)] as observed in Ref. [44]. Hence, onset of plasticity at room temperature occurs at $U = 0.75$ km/s. Impact at $U = 0.75$ km/s displays a distinct spike-valley feature at EPTW zone. When the piston is pushed at a higher velocity as in the case of 1.1 km/s [Fig. 2(c)], the spike-valley difference becomes less prominent. Further increase of impact strength enhances the disorder in the structure and turns the elastically overdriven target into a plastically overdriven one. Thus, investigation of

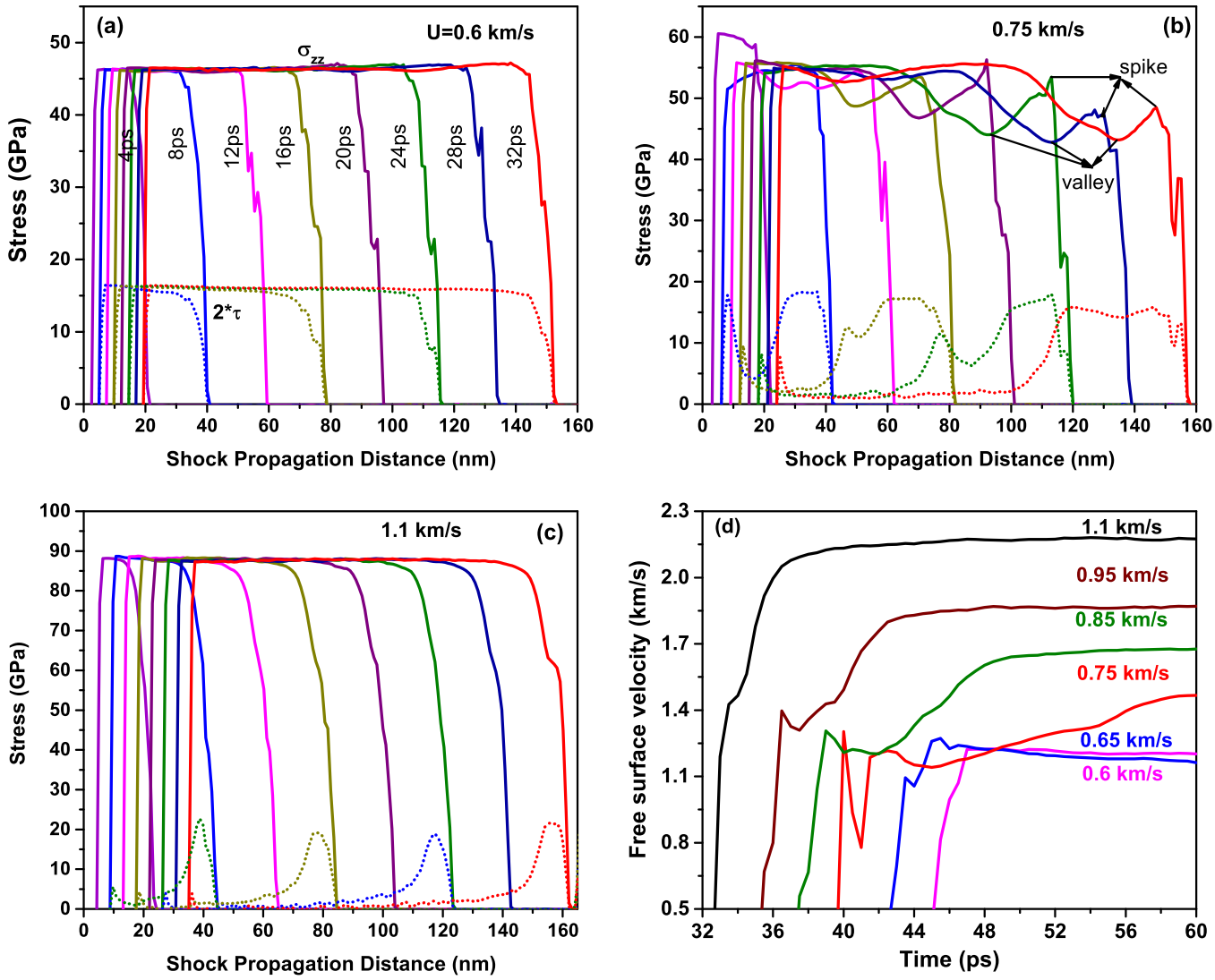

FIG. 2. Space-time evolution of stress wave from 4 ps to 32 ps within 165-nm sample for impact at (a) 0.6 km/s (b) 0.75 km/s (c) 1.1 km/s. Solid lines in each case show longitudinal stress σ_{zz} whereas dotted lines refer to shear stress 2τ. To decongest the figures, shear stresses are plotted at alternate times. (d) Time profile of particle velocity at free surface of 165-nm sample for various impact velocities. Time for elastic wave reaching free surface in all the cases is close to 32 ps, however, for clear observation of elastic kink we have shifted each curve by 2 ps.

HEL can be performed only within an intermediate range of impact velocities.

The EP feature of shock propagation can also be differentiated through spatial profile of shear stresses. Constant shear value of 6 GPa is maintained throughout the crystal for low velocity impact of $U = 0.6$ km/s, indicating pure elastic wave propagation. For $U = 0.75$ km/s, shear stress shows a dip at certain locations, evidence of plastic wave formation.

Decrease in shear stress associated with higher peak stress leads to dislocation initiation and formation of plastic fronts. This can be observed for higher U cases.

In Fig. 2(d), we show the FSV profile for six increasing values of impact velocities. Except $U = 0.6$ km/s, all other curves show an initial kink corresponding to elastic stress maximum, hereafter referred to as the *HEL spike*, followed by a valley region of varied width and depth arising due to stress relaxation, hereafter referred to as the *HEL valley*; and steady increase to final value corresponding to plastic wave propagation.

The appearance of spike and valley features of elastic waves was also reported for single as well as polycrystalline Ta [12,18,19,30]. Experiments of Pang *et al.* [18] on mm-size samples showed prominent maximum and minimum in elastic stress along the [001] direction and subdued features for [110] and [111] directions. The reason for the appearance of the spike is attributed to underlying physical mechanisms governing the dislocation motion, its mobility, and consequent stress relaxations due to accommodation of plastic strain [16,30].

The slope of velocity-time curves and hence plastic strain rate increases with increase in impact velocity from 0.65 km/s to 1.1 km/s.

Elastic and plastic waves are generally separated by a near-plateau region that indicates the time required for elastic to plastic wave transitions. Plateau width δt_p is a qualitative

measure of the difference between their respective wave velocities, U_{se} and U_s, and can be calculated as $\delta t_p = L_z(1/U_s - 1/U_{se})$.

For a particular length sample, δt_p reduces as the difference between propagation velocities of the elastic precursor front and plastic compression wave reduces. For elastically overdriven systems, the plastic wave speed is low; this makes larger δt_p as observed for low strength impact. As impact velocity is increased, the linear rise of the elastic wave speed and nonlinear rise in plastic wave speed leads to closing the time gap between the two waves. The squeezed EP feature in FSV profile as observed for 1.1 km/s of Fig. 2(d) indicates equalizing of speed for two types of waves.

A. Effect of system dimension on EPTW profile

NEMD simulation is generally facilitated by imposing periodic boundary condition at two orthogonal directions of simulation box wherein boundary atoms are assumed to interact with external ones. However, this is known to cause surface or boundary effects in estimates of physical parameters. For study of attenuation of longitudinal wave across a certain thickness, as is the interest of current paper, one has to consider the lateral dimensions in respect to length carefully. It is shown here that lateral dimension significantly affects stress relaxation behind the elastic front. To elucidate this phenomena, we introduce the *aspect ratio* defined as the box width to length ratio, i.e., $\mathrm{AR} = L_x/L_z = N_x/N_z$. Accordingly, shock simulation is carried out for varying ARs.

It is shown that a too-small value of the AR faces the problem of the boundary effect in relaxing the stress by mobile dislocations. Its manifestation is reflected in the spike-valley feature of the elastic front. The shallow valley region is an artifact of the low AR. It is thus prudent to carry out simulations for different ARs in an effort to converge HEL results before arriving at any conclusive trend. However, increasing system dimensions would increase the number of atoms nonlinearly, demanding exhaustive computing resources. Hence a trade-off between the two has been established.

1. *Sample length* $L_z = 165$ *nm*

The results presented in Fig. 2 are generated using $N_x = N_y = 100$ unit cells making $L_x = L_y = 33$ nm. In Fig. 3(a), we have illustrated the effect of increasing lateral size on FSV and stress profile of a 165-nm Ta sample for an impact velocity of 0.75 km/s. FSV results for seven different values of AR, i.e., 0.04, 0.06, 0.08, 0.1, 0.12, 0.16, and 0.2 corresponding to $L_x = 6.6,\ 10,\ 13.2,\ 16.5,\ 19.8,\ 26,\ 33$ nm clearly show the change in relative magnitude of particle velocity at spike-valley positions. As the AR is increased, even though the spike does not show significant deviation, but the valley becomes deeper. The spike and valley converges for AR = 0.2, corresponding to $L_x = 33$ nm. Further increase of the AR does not offer appreciable change. It is easy to find that the lower size box suffers from severe underestimation of FSV kinks for HEL valley and HEL spike. However, the difference is still not that serious for smaller size samples. Stress wave patterns shown as the inset of Fig. 3(a) correspond to AR = 0.2 (solid) and 0.06 (dashed) for four different time snapshots. It can be noticed that lateral size influences the spatial profile of stress, particularly in the EPTW region, making significant difference in stress attenuation at valley points.

2. *Sample length* $L_z = 660$*-nm*

The influence of lateral dimension on EPTW propagation is more severe for larger length samples as displayed in Fig. 3(d). For impact at 0.75 km/s, FSV profiles for lower values of the AR indicate a prolonged elastic part spanning for 40 ps before plastic rise takes place. However, as the AR is increased to 0.04, an elastic wave appears with usual signatures of spike and valley kinks. Absence of a valley region for a lower AR suggests negligible stress relaxation due to the unavailability of a sufficient number of atoms in a direction perpendicular to shock advancement. The spatial profile of the stress wave plotted for AR = 0.025 (dotted) and AR = 0.05 (solid), shown as the inset of Fig. 3(d), reflects the strong influence of lateral dimension on elastic wave patterns. Even for $L_x = 33$ nm, the convergence of spike-valley stresses as observed in shorter length samples could not be attained. To optimize computational times with the available resources, we have restricted to $L_x = 33$ nm without significant loss of accuracy.

Flow of pressure disturbance causes a formation of atomic layers adjacent to physical boundaries of the simulation box that grows with time. For a narrow-width box, this reduces the free flow cross-sectional area, thereby limiting the initiation of deviatoric stresses. This alters the flow from an initially inviscid to a well-developed viscous flow for low L_x boxes. A larger width box does not suffer from boundary layer influence.

Thus, solid Ta behaves like a viscoplastic medium wherein shear stress is proportional to plastic strain rate, with the proportionality constant being analogous to dynamical viscosity. Since the origin of the plastic wave is different, it is not affected due to such change in lateral dimension.

B. Determination of HEL from stress-wave profile

Dynamic yield stress indicates the limiting value of longitudinal stress that a material can withstand and beyond which it yields plastically. The yield point on the locus of individual strong shock induced final states is referred to as HEL. In accordance with impact velocity limits for which EPTW appear, HEL also has a range.

This section is devoted to estimation of HEL from space-time evolution of a stress wave, a method accessible to NEMD simulation only. This is realized by analyzing decay of elastic stress amplitude as shocks of different strength advances through certain thickness samples.

First, we consider a spatial profile of longitudinal stress along the z direction for $U = 0.75$ km/s as shown in Fig. 2(b). The shock propagation distances are captured from the position of spike and valley of elastic wave fronts corresponding to different time snapshots within 32 ps (time for reaching the free surface).

In Sec. III A, we have shown that magnitude of elastic stress at the spike and valley are strongly influenced by the AR. Consequently, it becomes inevitable to observe the progression of these features individually while examining HEL. Even though such features are also highlighted in experimen-

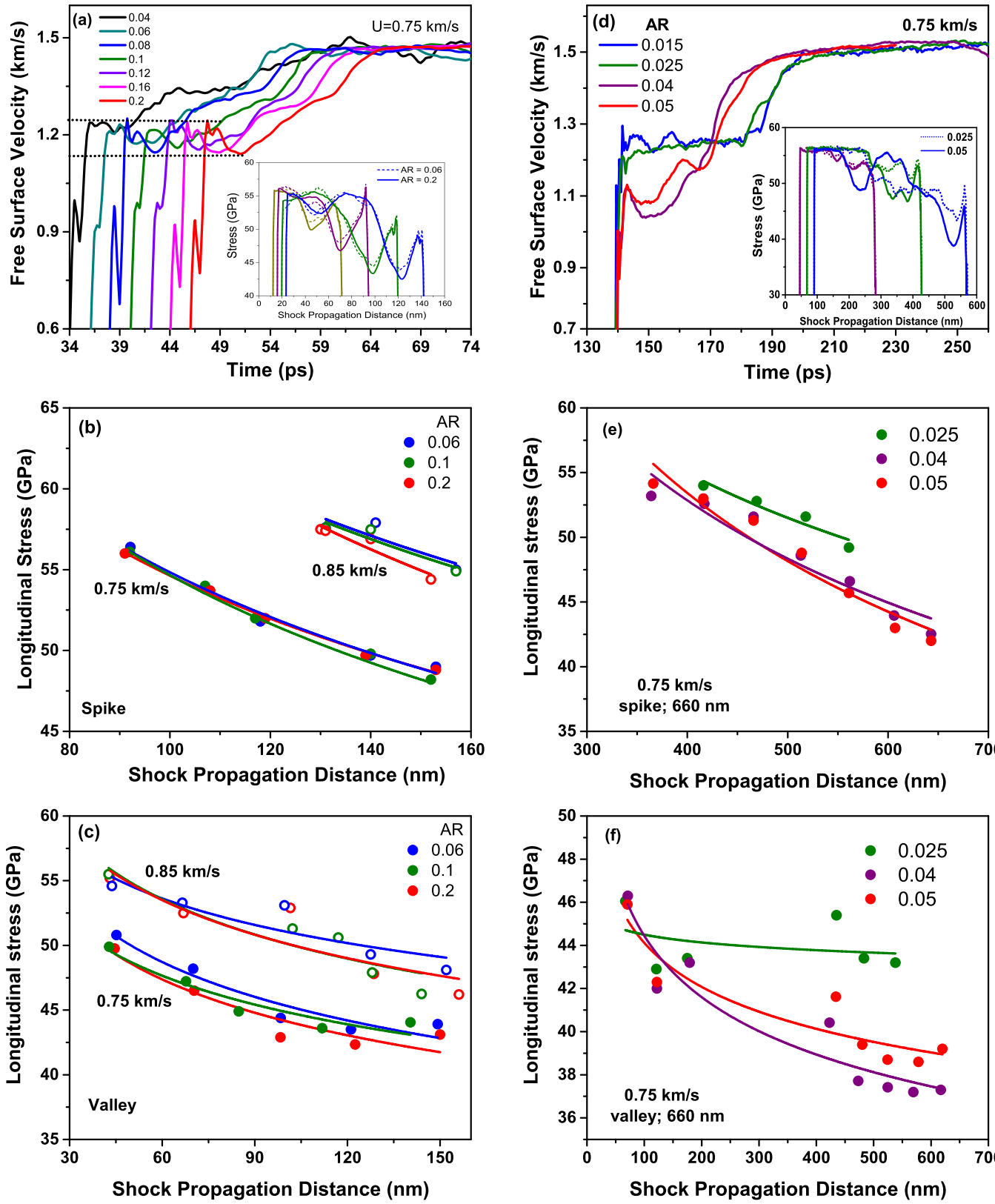

FIG. 3. Effect of aspect ratio on FSV profile of (a) 165-nm (time for elastic wave reaching free surface in all cases is close to 32 ps, however, for clarity of elastic kink we have shifted each curve by 2 ps.) (d) 660-nm sample for impact at 0.75 km/s. The corresponding stress profiles at 15, 20, 25, and 30 ps for 165-nm; and 60, 90, and 120 ps for 660-nm (shown from left to right), obtained with two aspect ratios are displayed in insets of (a) and (d), respectively. Elastic precursor decay for spike (b) and valley (c) positions corresponding to sample length of 165-nm for two impact velocities. Spike (e) and valley (f) stresses for 660-nm corresponding to $U = 0.75$ km/s. For four lower panels, symbols represent simulation data and solid lines refer to fitted curves according to Eq. (4).

TABLE I. Coefficients σ_0 and n of fitting function of Eq. (4) for elastic precursor decay of 165-nm and 660-nm samples at room temperature. Results pertaining to spike and valley points are listed for different aspect ratios.

U (km/s)	Location	L_x (nm)	AR	σ_0 (GPa)	n	L_x (nm)	AR	σ_0 (GPa)	n
		←	165-nm		→	←		660-nm	→
0.75	Spike	10	0.06	66.75	0.28	17	0.025	57.5	0.29
		17	0.1	67.7	0.31	26	0.04	55.75	0.39
		33	0.2	66.0	0.27	33	0.05	56.84	0.46
0.75	Valley	10	0.06	49.97	0.143	17	0.025	44.8	0.011
		17	0.1	48.69	0.12	26	0.04	47.48	0.095
		33	0.2	48.57	0.138	33	0.05	46.25	0.068
0.85	Spike	10	0.06	75.21	0.26	17	0.025	68.92	0.685
		17	0.1	75.52	0.275	26	0.04	57.64	0.425
		33	0.2	79.84	0.34	33	0.05	64.5	0.52
0.85	Valley	10	0.06	54.57	0.095	17	0.025	58.2	0.135
		17	0.1	54.84	0.129	26	0.04	56.54	0.123
		33	0.2	54.74	0.126	33	0.05	60.79	0.195

tal work by Zaretsky and Kanel [19], due attention has not been paid to studying the role of spike-valley characteristics in HEL decay pattern.

We denote the stress at which EP transition occurs at a particular distance as σ^s_{HEL}. It corresponds to HEL of that thickness sample. For quantitative estimation of HEL decay, following Ref. [19], we have fitted σ^s_{HEL} versus z data with an empirical function given by

$$\sigma^s_{\mathrm{HEL}} = \sigma_0 (z/z_0)^{-n}. \tag{4}$$

In the above, z_0 refers to the position of the first appearance of EPTW splitting. Dynamic yield strength is directly proportional to HEL stress.

C. Effect of system dimension on HEL decay

From the above displayed features of a stress wave pattern and its signatures in the FSV profile of Figs. 3(a) and 3(d), it becomes evident that the AR of the simulation box significantly influences the elastic precursor decay. Elastic stress values at spike and valley points for three different ARs corresponding to $L_x = 10$, 17, and 33 nm with $L_z = 165$ nm are recorded from the spatial profile of stress and shown by filled ($U = 0.75$ km/s) and open ($U = 0.85$ km/s) symbols of Figs. 3(b) and 3(c). The corresponding results for $L_z =$ 660-nm with $L_x = 17$, 26, and 33 nm due to the impact at 0.75 km/s are shown in Figs. 3(e) and 3(f). The data for individual AR cases are fitted with the decay law of Eq. (4) as shown by solid lines. The fitting constants arising for three respective AR values are listed in Table I.

It can be noticed that for a particular impact, elastic stress decay rate is more for the spike (higher values of n), but it attenuates rather slowly for valley points. Moreover, spike stress decay rates for the 660-nm sample is higher as compared to the 165-nm case. Obvious fluctuations of valley stress decay for 660-nm is an artifact of the inadequate lateral dimension considered in this case. Thus elastic stress versus distance data leads to different decay profiles for spike and valley points.

A closer look into Figs. 3(b), 3(c) 3(e), and 3(f) conveys that the strength of Ta single crystal reduces with increasing lateral dimension, a trend known as size effect [61–63]. A similar study of cross-section dependence on spall strength for Ta single crystal was also reported [64]. The decrease of spike in propagating the elastic wave is caused due to reduced magnitude of the strain rate at which it is loading. This occurs due to attenuation of available energy in the incoming wave.

Since strain-rate reduction for smaller width samples is not much, hence significant reduction in HEL spike is not expected. On the contrary, decrease in the valley region appears to be more prominent as it represents the stress relaxation on initiation of dislocation nucleation and growth in pure crystal.

In the current paper, thus we have proposed different decay laws for the HEL spike and valley and investigated the influence of lateral dimension of the simulation box on yield strength.

The experimental work of Zaretsky and Kanel [19] led to the following HEL decay law:

$$\sigma_{\mathrm{HEL}} = 1.45(z/z_0)^{-0.7}, \tag{5}$$

where z is the propagation distance in mm, $z_0 = 1$ mm and $\sigma_0 = 1.45$ GPa. The higher decay rate ($n = 0.7$) as compared to single crystal values of $n \approx 0.3$ (refer to Table I) in our study can be attributed to three main contributing factors: (i) low impact velocity or loading stress associated with low plastic strain rates ($10^4 - 10^6\ \mathrm{s}^{-1}$), (ii) polycrystalline samples used in that experiment, and (iii) use of HEL data pertaining to different sample temperatures of 300 K, 800 K, and 1300 K in arriving at the above fitting relation. However, fitting experimental HEL data of Razorenov *et al.* [22] belonging to strain rate of $10^6\ \mathrm{s}^{-1}$ with Eq. (4) provides $n = 0.37$ for course grain and $n = 0.33$ for ultrafine grain samples. This is in overall agreement with decay rates obtained in our simulation.

IV. ANALYSIS OF HEL FROM FREE SURFACE VELOCITY PROFILE

In situ observation of stress evolution with the advancement of shock is not possible in experiments. In this regard, the FSV profile plays a significant role as it indicates

TABLE II. Comparison of HEL calculated from stress attenuation and FSV profiles for 165-nm and 660-nm Ta single crystals at 300 K. Compilation refers to simulations with $L_x = 33$ nm.

U (km/s)	σ_{zz} (GPa)	C'_L (km/s)	L_z (nm)	$\sigma^s_{\rm HEL}$ (GPa)	$\sigma^2_{\rm HEL}$ (GPa)	$\sigma^1_{\rm HEL}$ (GPa)	$\sigma^s_{\rm HEL}$ (GPa)	$\sigma^2_{\rm HEL}$ (GPa)	$\sigma^1_{\rm HEL}$ (GPa)
				←	Spike	→	←	Valley	→
0.75	55.0	4.80	165	48.0	48.0	40.5	42.7	45.9	38.73
			660	42.0	43.97	37.09	38.8	42.35	35.73
0.85	62.0	4.83	165	55.0	53.0	44.24	46.2	49.7	40.84
			660	43.9	47.22	38.79	36.0	40.59	33.35
0.95	73.6	4.85	165	55.4	57.92	47.30			
			660	56.7	59.17	48.32			
1.1	87.7	4.90	165	58.6	58.93	48.32			
			660	58.2	59.76	49.0			

shock-induced microstructual changes including phase transition, EP transition, spalling, etc. in a sample. Next, following experimental methods, we evaluate $\sigma_{\rm HEL}$ from time variation of FSV. HEL can be determined as [19]

$$\sigma_{\rm HEL} = \tfrac{1}{2}\rho_0 U_{se} U_{fe} \tag{6}$$

where ρ_0 is ambient density of the material, U_{se} is the pressure-dependent elastic wave velocity, and U_{fe} is FSV at the precursor front, which is double the particle velocity just before shock unloading. The distinct spike and valley feature is associated with different values of FSV kink, i.e., U_{fe}. U_{se} in most of the experimental work with mm-size samples is replaced by longitudinal wave velocity C_L without loss of accuracy. However, this introduces some difference, particularly for high loading pressures and small system dimensions as illustrated below. To differentiate the scenario, we introduce two expressions for HEL as given below:

$$\sigma^1_{\rm HEL} = \tfrac{1}{2}\rho_0 C_L U_{fe} \tag{7}$$

and

$$\sigma^2_{\rm HEL} = \tfrac{1}{2}\rho_0 C'_L(P,T) U_{fe}. \tag{8}$$

Thus, $\sigma^1_{\rm HEL}$ refers to HEL estimated from the FSV profile using elastic wave speed U_{se} at normal pressure and temperature (300 K), which is C_L itself; and ambient density of Ta at 300 K. The second definition $\sigma^2_{\rm HEL}$ corresponds to corrected elastic wave speed at prevailing pressure and temperature, i.e., $U_{se} = C'_L(P,T)$. Moreover, in Eq. (8), the density corresponds to the initial sample temperature for which HEL is being obtained. In the current paper, longitudinal wave velocity $C'_L(P,T)$ is calculated from time variation of the elastic front position in stress/particle velocity obtained in NEMD simulations. Considering HEL estimated from decay of elastic stress expressed by Eq. (4) of Sec. III B as a reference, we find the relative deviation from that obtained by FSV, with and without pressure-temperature dependence in elastic wave speed. To that end, we define relative deviations as

$$\Delta\sigma_1 = \left|\frac{\sigma^1_{\rm HEL} - \sigma^s_{\rm HEL}}{\sigma^s_{\rm HEL}}\right|, \quad \Delta\sigma_2 = \left|\frac{\sigma^2_{\rm HEL} - \sigma^s_{\rm HEL}}{\sigma^s_{\rm HEL}}\right|. \tag{9}$$

U_{fe} values associated with spike and valley positions are picked from Fig. 2(d) for the $L_z = 165$ nm sample and AR = 0.2. Taking $C_L = 4.1$ km/s, HEL from the spike and valley position as listed in Table II is found to be 40.5 and 38.73 GPa, respectively, for piston velocity of 0.75 km/s. This can be compared with 48.0 and 42.7 GPa obtained from spike and valley data of stress-wave analysis. However, if P-T dependence in C_L is considered, then using $U_{se} = C'_L = 4.8$ km/s for 55 GPa (due to impact at 0.75 km/s) and $T = 300$ K in Eq. (8), HEL increases to 48.0 and 45.9 GPa for the two points, respectively.

Hence, prediction of a HEL spike by modified elastic wave speed is in excellent agreement with that estimated from elastic stress decay. Relative deviations for the HEL valley are $\Delta\sigma_1 = 9.3\%$ and $\Delta\sigma_2 = 7.5\%$. A similar exercise is carried out for a larger sample length of $L_z = 660$-nm. Intercomparison among different estimates of HEL are presented in Table II.

V. INFLUENCE OF INCREASING IMPACT STRENGTH

It is clear from Fig. 2(d) that with the increase in impact velocity, the elastic kink appears for higher particle velocities, suggesting higher values of HEL. In this section, we extend the stress wave and FSV analysis of HEL determination for higher impact velocities and hence strain rates.

Consolidated results for HEL estimated from the stress wave profile $\sigma^s_{\rm HEL}$ and two approaches of FSV-based values, $\sigma^1_{\rm HEL}$ and $\sigma^2_{\rm HEL}$, with respect to spike and valley points are presented in Table II. The table also compares HEL of two different length samples of 165- and 660-nm Ta. The peak stresses associated with each impact and corresponding longitudinal wave velocities are also listed in Table II.

To establish a trend, in Fig. 4(a) we have plotted $\sigma_{\rm HEL}$ of a 165-nm sample as a function of impact velocity. Study reveals that HEL increases with impact strength. It can be noticed that for all impact cases, $\sigma^2_{\rm HEL}$ lies close to $\sigma^s_{\rm HEL}$, whereas $\sigma^1_{\rm HEL}$ falls quite away from $\sigma^s_{\rm HEL}$. This makes $\Delta\sigma_2$ to lie within 10%, whereas $\Delta\sigma_1$ is as large as 20%. As expected, for all impact velocities, HEL of the 660-nm sample (single case shown) is less than the 165-nm one.

FSV plot for different impact strengths [Fig. 2(d)] provides good information about plastic strain rates. Plastic deformation rise time increases with U, thereby making the curves steeper for higher piston speed. It is shown that the slope of the plastic front increases very rapidly with shock strength. To that end, we define strain rate as $\dot{\varepsilon} = \dot{u}_{fsv}/2U_s$, where U_s is

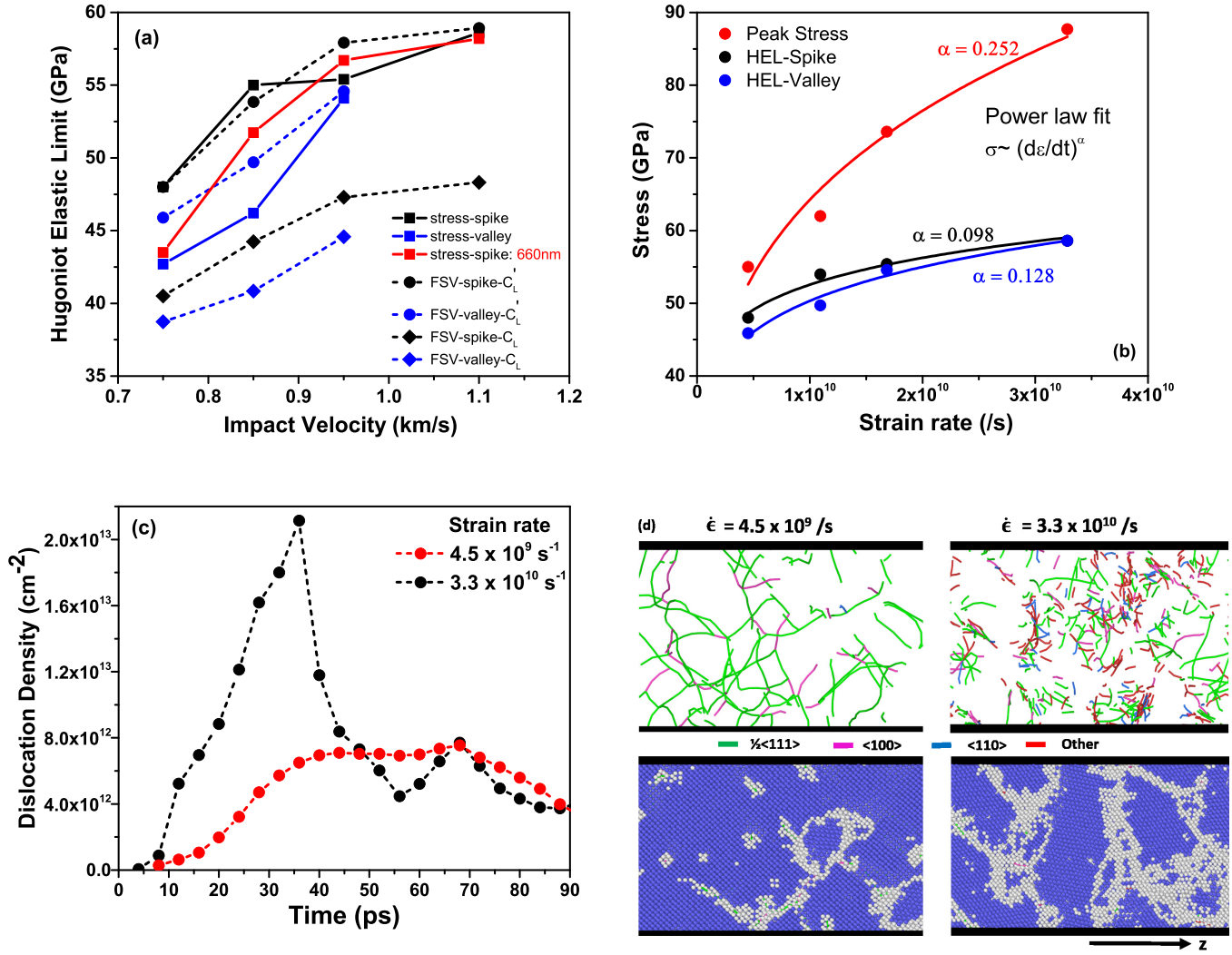

FIG. 4. (a) Effect of increasing impact velocity on three estimates of HEL for 165-nm target. Single case of 660-nm is also included. (b) Variation of peak stress and two estimates of HEL, namely, spike and valley, with strain rate. Solid lines refer to power-law fitting in the given form. The exponents in each case are shown. (c) Time evolution of dislocation density for varying strain rates, red and black curves refer to impact at 0.75 and 1.1 km/s. (d) Dislocation structure formed at 32 ps: (top) dislocation lines calculated with DXA algorithm and colored based on their character: green for screw and magenta for edge segments; (bottom) atomic structure: blue shaded atoms refer to bcc structure and grey corresponds to dislocations or other lattice defects.

plastic wave speed and $\dot{u}_{fsv}$ is acceleration of the free surface just before plastic saturation is attained. We have calculated this quantity for the room temperature Ta target for $U = 0.75$, 0.85, 0.95, and 1.1 km/s. The results for peak stress versus strain rate data are shown in Fig. 4(b) (symbols).

Motivated by the universal character of steady shock waves in solids and the fourth power law as emerging from a series of experiments [65], we have fitted σ_{zz} versus $\dot{\varepsilon}$ with a generalized power law function given below:

$$\sigma_{zz} = \sigma_r \left(\frac{\dot{\varepsilon}}{\dot{\varepsilon}_0}\right)^{\alpha}. \tag{10}$$

The exponent α in our case turns out to be 0.251 with 9% fitting error. This shows very good agreement with the fourth power variation of strain rate with stress, i.e., $\dot{\varepsilon} \propto \sigma_{zz}^4$, as found for many metals [66]. The fitting constant σ_r implies stress at reference strain rate $\dot{\varepsilon_0} = 10^9\ \mathrm{s}^{-1}$ and its value is 36.1 GPa. Our study thus reveals that the universal relationship between Hugoniot stress and strain rate as deduced for strain rates ranging from $10^4\,\mathrm{s}^{-1}$ to $10^7\,\mathrm{s}^{-1}$ remains valid even in the extended regime of $10^9 - 10^{10}\ \mathrm{s}^{-1}$.

In Fig. 4(b), we have also shown HEL data obtained from stress wave decay for each peak stress. Like peak stress, spike and valley data of HEL stress are fitted with similar power-law variations of generic form:

$$\sigma_{\mathrm{HEL}-sp,val} = \sigma_0^r \left(\frac{\dot{\varepsilon}}{\dot{\varepsilon}_0}\right)^{\alpha}. \tag{11}$$

The fitting constant α corresponding to spike and valley are 0.098 and 0.128, respectively. Thus comparable rise of HEL with strain rate is exhibited for both locations. The values of σ_0^r, i.e., 41.95 GPa and 37.3 GPa, represent spike and valley HEL for the 165-nm sample subjected to strain rate of $\dot{\varepsilon_0} = 10^9\,\mathrm{s}^{-1}$.

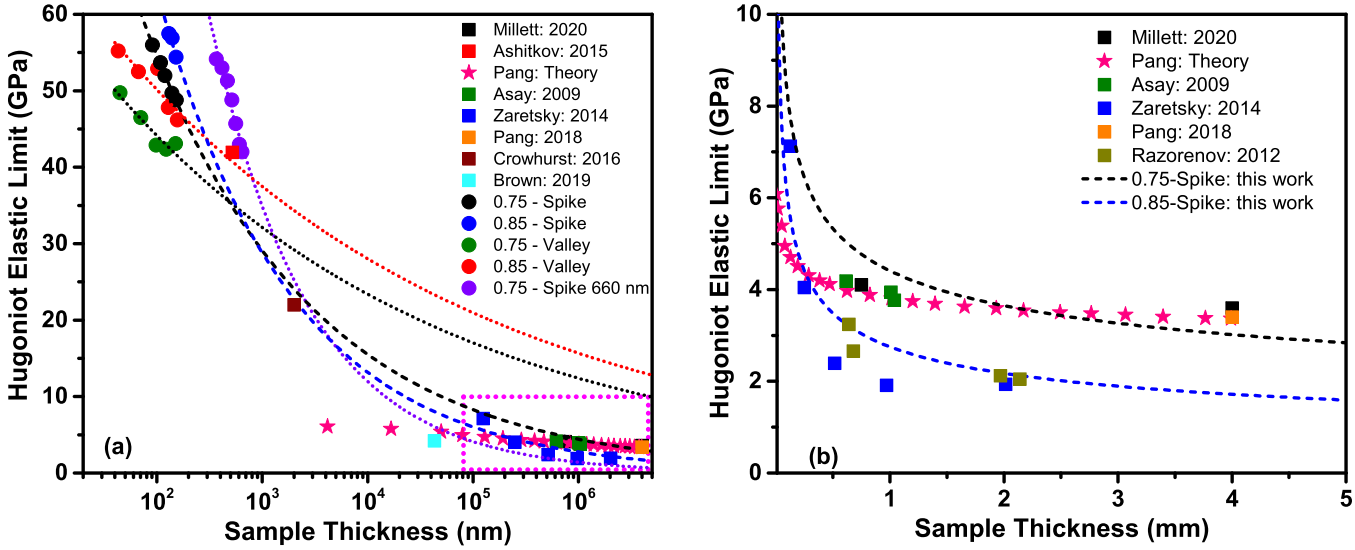

FIG. 5. Comparison of HEL with sample thickness from our model and available experiments. Upper panel shows the comparison for wide range of sample thickness whereas lower panel displays the same in narrow range. Black ($U = 0.75$ km/s) and blue (0.85 km/s) symbols: HEL-spike of our simulation ($L_z = 165$ nm). Black and blue dashed lines: Extrapolated decay law [Eq. (4) with coefficients of Table I]. Green (0.75 km/s) and red (0.85 km/s) symbols: HEL valley of our simulation. Green and red dotted lines: Extrapolated decay law. Violet symbol with dashed line: HEL spike with ($L_z = 660$-nm) and decay law with coefficients of Table I. Millett *et al.* [12]: Shock (gas gun) experiment on [001] single crystal. Ashitkov *et al.* [25]: Laser shock experiment. Red star: Theory [18], Asay *et al.* [20]. Ramp (magnetic loading) experiment. Zaretsky and Kanel [19]: Shock (gas gun) experiment. Pang *et al.* [18]: Shock (gas gun) experiment on [001] single crystal. Crowhurst *et al.* [26]: Laser shock experiment. Brown *et al.* [23]: Ramp (gas gun) experiment.

High strain rate is known to play a crucial role in plastic deformation modes, which is predominantly dislocation nucleation and motion in the case of [001] orientation. Plastic deformation in terms of mobile and immobile dislocations in shock-compressed Ta has been studied recently by developing a dynamic strength model applicable for strain rates up to 10^7 s^{-1} [67]. For quantitative illustration of the strain rate induced effect, time evolution of total dislocation density for two different impact strengths of $U = 0.75$ and 1.1 km/s with prevailing strain rates of $\dot{\varepsilon} = 4.5 \times 10^9$ and $\dot{\varepsilon} = 3.3 \times 10^{10}$ s^{-1}, respectively, are displayed in Fig. 4(c). In both cases, dislocation density increases with time and reaches maximum at 35 ps for $\dot{\varepsilon} = 4.5 \times 10^9$ s^{-1} and at 44 ps for $\dot{\varepsilon} = 3.3 \times 10^{10}$ s^{-1}, and thereafter reduces due to shock unloading. Note that for one order increase in $\dot{\varepsilon}$, the total number of dislocations per unit volume has raised from 10^{12} cm^{-2} to 10^{13} cm^{-2}. Observed increase of dislocation density with strain rate is in accordance with Orowan's law. Rapid rise of dislocations in the case of 1.1 km/s is a signature of a higher speed of dislocation motion. Relatively lower dislocation velocity causes the plateau region for lower impact strength.

Dislocation lines along with atomic configurations around the plastic front for two impact cases are displayed in visualization plots of Fig. 4(d). Note the major dislocations generated during shock propagation in the [001] direction. The lattice resistance for the motion of screw dislocations in bcc Ta is very high compared to the resistance of edge dislocation motion [68]. This is attributed to the observed dominance of screw dislocations over edge in Fig. 4(d). Edge and screw dislocations are types of line defects in crystal lattices. Edge dislocation occurs when an extra plane(s) of atoms is inserted or removed into a regular crystal, while the screw dislocation is associated with shearing deformational shift along a regular plane.

Dislocation analysis confirms the crystal plasticity and thereby supports the EPTW stress-based inferences presented in earlier sections.

VI. COMPARISON OF ROOM TEMPERATURE HEL WITH EXPERIMENTAL RESULTS

Owing to the small length scales involved in MD simulation, the results cannot be directly compared with experimental (gas gun) data largely belonging to mm-thick samples at lower strain rates ($10^3 - 10^6$ s^{-1}). However, in the present paper, a successful attempt has been made for validating experimental data by extrapolating elastic stress decay law established from MD simulations of submicron-thick samples along with strain-rate dependence of HEL derived in the previous section.

To that end, we have extrapolated the decay law constructed for 0.75 km/s and 0.85 km/s pertaining to spike and valley HEL of 165-nm sample and displayed for a wide range of thicknesses varying from 50 nm to 5 mm in Fig. 5. Available experimental data from micron to mm range with strain rate ranging from $10^4 - 10^9$ s^{-1} are embedded in this figure. For the sake of completeness, a single case of spike decay law for a 660-nm sample ($U = 0.75$ km/s) is also shown. For better comparison, the marked regime of Fig. 5(a) is shown in Fig. 5(b).

It can be observed from Fig. 5(a) that for micron-size samples, available experimental data of HEL corresponding to laser-driven shocks for 800 nm [25] and 2 μm [26], as well as gas gun driven shock for 43 μm [23] are in close agreement

TABLE III. Comparison of experimental HEL data with our simulation results using stress wave decay law without [Eq. (4)] and with [Eq. (12)] strain rate induced effect.

Thickness (mm)	Source	Ref-HEL (GPa)	HEL-Sp (GPa)		HEL-Val (GPa)	
			Eq. (4)	Eq. (12)	Eq. (4)	Eq. (12)
0.002	Ref. [26]	22.0	33.65	21.39	34.42	26.45
0.043	Ref. [23]	4.2	13.37	4.99	24.85	9.9
0.75	Ref. [12]	4.1	5.67	1.36	17.06	3.78
4.0	Ref. [12]	3.6	3.45	0.83	13.7	3.04
0.25	Ref. [19]	4.0	7.88	2.17	19.72	5.27
1.0	Ref. [19]	1.9	5.2	1.14	16.43	3.24
1.148	Ref. [69]	2.8	6.05	2.51	14.32	6.3
4.488	Ref. [69]	2.4	4.19	1.74	11.87	5.2

with our results. Figure 5(a) conveys that HEL-valley decay law obtained from 165-nm for both impacts causes significant overestimation of room temperature HEL data with respect to experimental ones. HEL of [001] single crystal Ta estimated by Pang *et al.* [18] (orange square) agrees well with our extrapolated spike decay law. Taking an average of two impact cases, HEL for 1-mm-thick samples turns out to be 5.2 and 16.43 GPa from extrapolated decay law of spike and valley, respectively, which is a significant overestimation of reference HEL (1.9 GPa [19]). We conjecture that the probable reason for this deviation is the strain rate induced effect. By simple extrapolation of the spatial decay law of HEL given in Eq. ,4 we can predict the strength of a mm-thick target subjected to dynamic loading with $\dot{\varepsilon} \geqslant 10^9$ s^{-1} only.

It is known that plastic strain rate reduces as the shock front moves forward within the target thickness. Essentially for the same impact, strain rate decreases as target thickness is increased. However, NEMD simulation of shock propagation cannot encompass such a wide range of sample thicknesses and hence encountering very low strain rates of an experimental regime would be difficult. The lowest strain rate in our simulation is $\approx 10^9$ s^{-1}, at least four orders of magnitude higher than Ref. [19]. To bridge the gap, we have segregated the length and strain-rate dependence of HEL and assumed the combined effect as convolution of individual effects of these two parameters. Under this assumption, we write

$$\sigma_{\mathrm{HEL}} = \sigma(\dot{\varepsilon}) \times \sigma(z) = \sigma_0\, \sigma_0^r \left(\frac{\dot{\varepsilon}}{\dot{\varepsilon}_0}\right)^{\alpha} \left(\frac{z}{z_0}\right)^{-n}. \quad (12)$$

Utilizing this formulation, we estimate the HEL spike and HEL valley for sample thicknesses used in the experiment of Refs. [12,19,23,26,69] as presented in Table III. For illustration, taking the example of Ref. [19], we observe that use of Eq. (12) brings HEL for a 1-mm target ($\dot{\varepsilon} \approx 10^4$ s^{-1}) from 5.2 to 1.14 GPa for spike and 16.43 to 3.24 GPa for valley. These are in close agreement with the reported experimental value of 1.9 GPa.

From the experimental data presented in Table III, it can be observed that spatial decay extrapolation [Eq. (4)] alone causes an overestimation of HEL for μm- to mm-thick samples (spike: less and valley: more). But subsequent use of strain rate correction [Eq. (12)] brings down the HEL values in the range comparable to experimental results. This proves the robustness of our formulation.

VII. HEL FOR HIGHER SAMPLE TEMPERATURES

Shock-wave study at elevated sample temperatures enables one to know the material strength and plastic deformation mechanisms at varied strain rates. Most of the earlier studies on Ta have addressed temperature variation of yield strength much below melting, while very few consider the variation at still higher temperatures where the deformation process is controlled by diffusion. In this section, we analyze the role of the initial sample temperature in altering the dynamic strength of Ta single crystal. The effect of enhanced thermal stimulation on dislocation dynamics is also analyzed.

A. Effect of temperature on elastic precursor decay

In contrast to phenomena observed at room temperature, we find that lateral dimension does not cause an appreciable difference at higher sample temperatures as illustrated in Fig. 6. Figure 6 displays FSV profiles obtained from simulation of two different length samples initially at 1500 K impacted at 0.75 km/s considering $L_x = 10$, 17, and 33 nm. It is obvious from Fig. 6(a) that profiles for shorter length samples neither exhibit distinct spike-valley signatures nor change significantly with increase in AR. However, for larger sample lengths, we find that different AR values causes a significant deviation in the appearance of spike-valley kinks as seen in Fig. 6(b). Our simulation also confirmed that this deviation reduces drastically as loading speed is increased.

Elastic stress values picked from stress-wave evolution for two different sample lengths are shown as the inset of Fig. 6 (symbols). Respective data for three values of AR are fitted with Eq. (4) and are shown by solid lines.

Note that increase in the AR has caused a stable decay pattern for both L_z cases, making a standardized prediction of σ^s_{HEL} from the stress-wave profile. Rest of all the thermal analysis are carried out considering $L_x = 33$ nm for both L_z cases.

The initial sample temperature is now increased systematically from 300 K to 3100 K. For impact at 0.75 km/s, the elastic stress at spatial points where EPTW splits in the

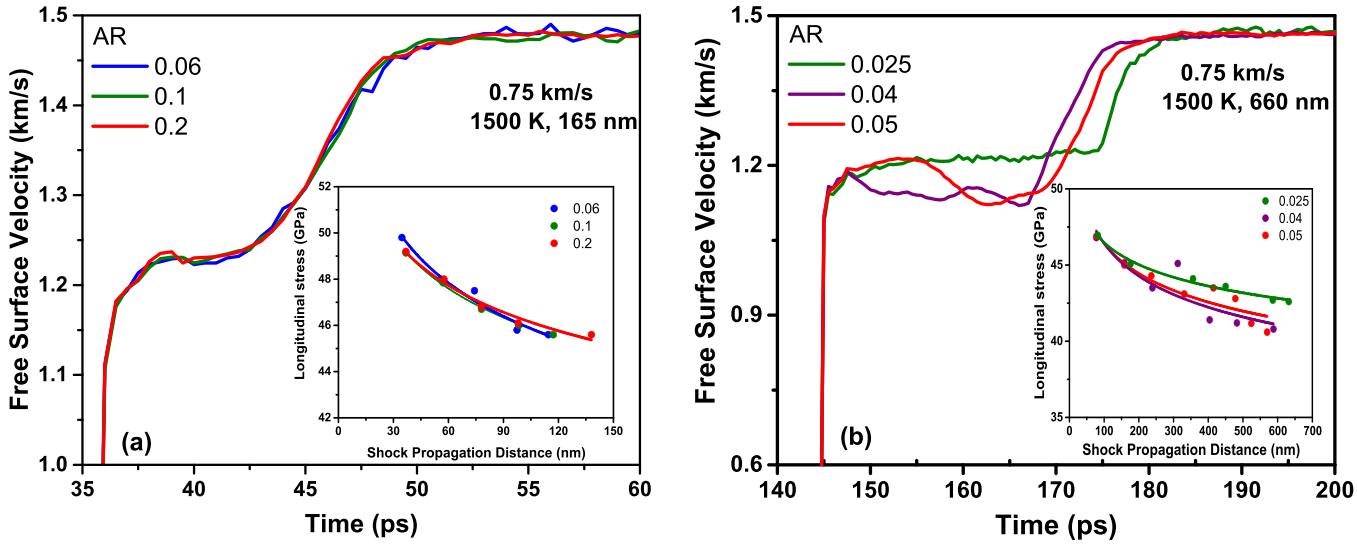

FIG. 6. FSV profile of (a) 165-nm and (b) 660-nm Ta single crystal, initially at 1500 K, due to impact at 0.75 km/s plotted for lateral dimension, $L_x = 10, 17, 33$ nm. Insets in both panels show maximum elastic stress as a function of distance. Symbols refer to simulated data captured from spatial profile of stresses calculated for displayed values of AR. Solid lines are fitted curves according to Eq. (4).

165-nm sample as observed for different initial temperatures is presented by symbols of Fig. 7(a). The corresponding decay fits according to the empirical relation of Eq. (4) are shown by solid lines. The trend of HEL with increasing temperature can be inferred by analyzing the variation of fitting coefficients σ_0 and n as shown in Fig. 7(b). It can be noticed that the decay rate n is very high at room temperature; it drastically reduces by one order even for 600 K. The minimum elastic stress attenuation rate indicates a higher value of HEL at this temperature. For $T > 600$ K, the decay rate shows a marginal increase with temperatures up to $0.5T_M$ (T_M is the melting point of Ta at ambient pressure) and remains almost constant beyond that. In the same way, the magnitude of σ_0 is very high at 300 K and exhibits a sharp reduction with slight increase in temperature to 600 K. Decrease in σ_0 is rather slow for $T > 0.5T_M$. T_M is found to be 3350 K by one-phase MD simulations carried out by us using the Ta1 potential, as against the experimental value of 3282 K [70].

A similar study for HEL decay at higher sample temperatures was reported for fcc metals Cu [46] and Al [48]. However, it was shown that as temperature increases, σ_0 increases whereas n decreases, which is in contrast to the observed thermal behavior of Ta where both the parameters reduce with temperature. The elastic precursor of fcc Ag showed increasing n with temperature [45].

B. Effect of temperature on HEL

To explain the thermal influence of HEL, in Fig. 8 (left panel) we display the FSV profile obtained due to impact at 0.75 km/s for different sample temperatures. It can be noticed that the spike-valley feature occurs only for low temperatures.

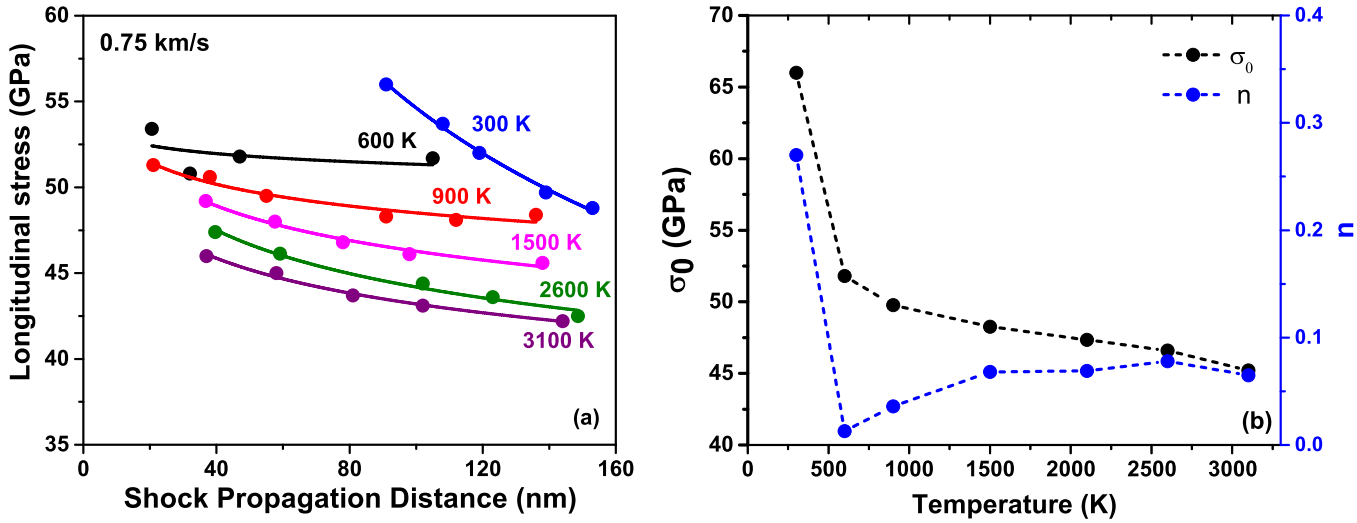

FIG. 7. (a) Characteristics of elastic precursor decay for different sample temperatures. Symbols represent values of stress at the EP transition point and solid lines refer to fitting curves with Eq. (4). (b) Temperature variation of decay fitting parameters, σ_0 and n.

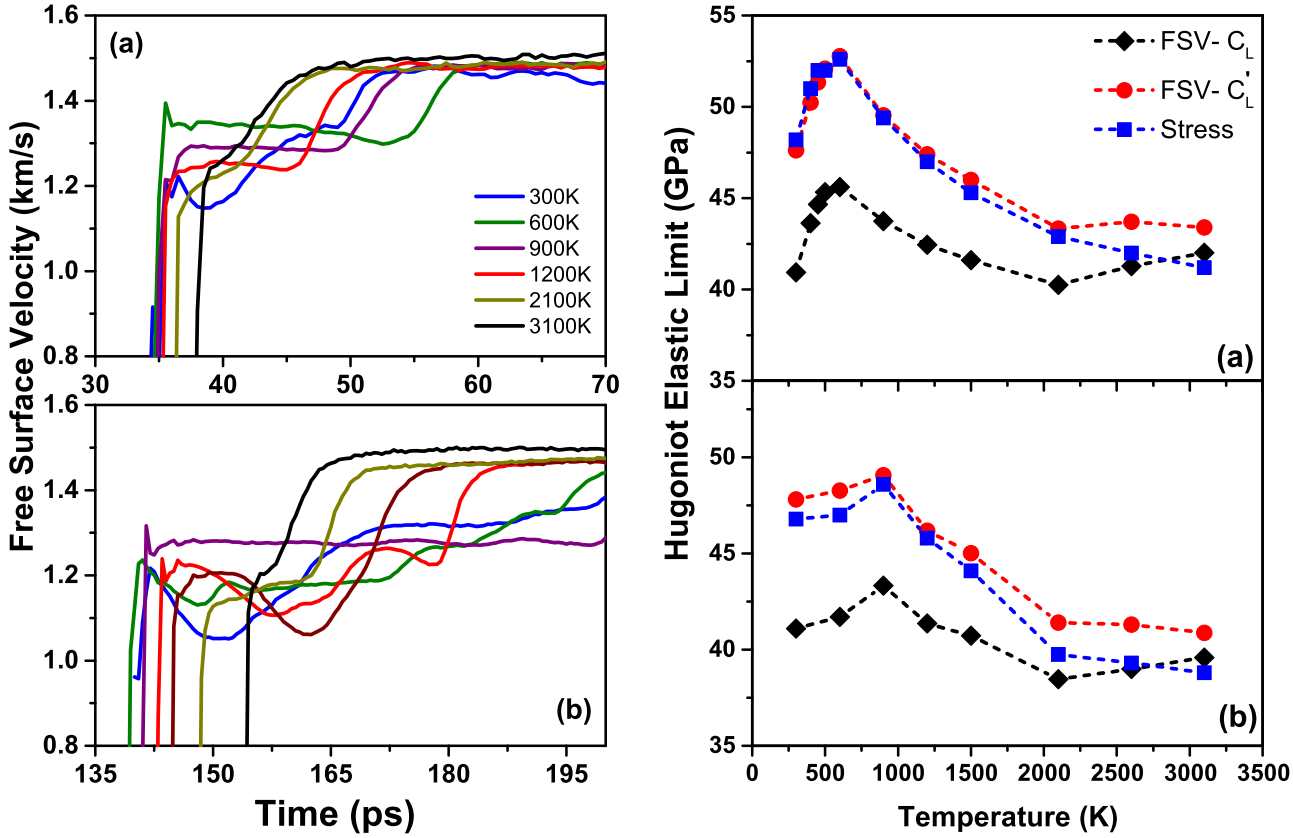

FIG. 8. Left: Time variation of FSV arising due to impact at 0.75 km/s on (a) 165-nm and (b) 660-nm Ta samples initially at 300 K, 600 K, 900 K, 1200 K, 2100 K, and 3100 K. Right: Temperature dependence of HEL for same length samples. HEL calculated from stress wave profile, FSV profile using C_L']Eq. (8)] and C_L [Eq. (7)] are shown by blue, red, and black symbols. Dashed lines serve as guides for the eye.

As the shock wave propagates through the high-temperature medium, the spike feature gets less pronounced and levels with the valley. The existence of defects and dislocations in the preheated sample is mainly responsible for this. Hence, for all thermal analysis, we talk only about HEL without distinguishing between the two.

For the 165-nm sample [curve, Fig. 8(a)], the elastic kink rises from 300 K to 600 K and then decreases with further increase of temperature. The maximum in the elastic kink for 660-nm shifts to 900 K [curve, Fig. 8(b)]. Using particle velocity at the elastic kink, we now calculate $\sigma^1_{\rm HEL}$ and $\sigma^2_{\rm HEL}$ that makes use of longitudinal wave velocity at ambient and prevailing pressure-temperature conditions, i.e., C_L and C_L'. These two estimates of HEL are compared with those obtained from stress profiles in Fig. 8 (right panel). All three estimates of HEL exhibit a similar profile. The maximum strength (highest HEL) for 165- and 660-nm samples occur at 600 K and 900 K, respectively. Thus for bcc Ta, our simulation indicates a substantial increase of the rate sensitivity at low temperature. It follows that coupling between temperature and strain rate is crucial for correct interpretation of transition between athermal and thermally activated processes of plastic deformation at low temperature and at high strain rates.

It can be noticed from the right panels of Figs. 8(a) and 8(b) that for all temperatures, HEL estimated from the FSV profile using C_L' agree very well with stress profile values. Except at very high temperatures, $\sigma^1_{\rm HEL}$ maintains a constant deviation from both $\sigma^2_{\rm HEL}$ and $\sigma^s_{\rm HEL}$. Relative deviation $\Delta\sigma_2$ for both sample sizes are limited to 2% whereas $\Delta\sigma_1$ is about 15% for entire temperature range. This leads us to conclude that for submicron-size samples at extremely high strain rates, temperature- and pressure-dependent longitudinal wave velocity provides a correct estimation of HEL.

C. Thermal effect at higher strain rates

Next we explore HEL for elevated sample temperature at higher strain rates. This is accomplished by impacting the 165-nm sample at two higher velocities of 0.85 km/s and 0.95 km/s. FSV histories for these two cases plotted in Fig. 9 provides good guidance for observed pattern. Two cases of subnormal temperatures ($T = 20$ K and 100 K) are also shown in the figure. As can be seen, for a particular impact velocity, separation between the elastic and plastic zone reduces with increase in T. At very high temperature, the EPTW zone shrinks to a single point. Depending on impact strength, beyond a certain high initial temperature, the crystal responds only plastically. As impact strength increases, absence of the EPTW zone, an indicator for pure plastic transition, occurs for lower temperature. Figures 9(a) and 9(b) clearly convey that the maximum temperature for which HEL can be determined for $U = 0.85$ and 0.95 km/s are 2100 K and 1500 K. Beyond this temperature, material is fully plastic.

With these observations, next we analyze the overall behavior of HEL for a wide range of temperatures varying from 20 K to melting, difficult to explore experimentally.

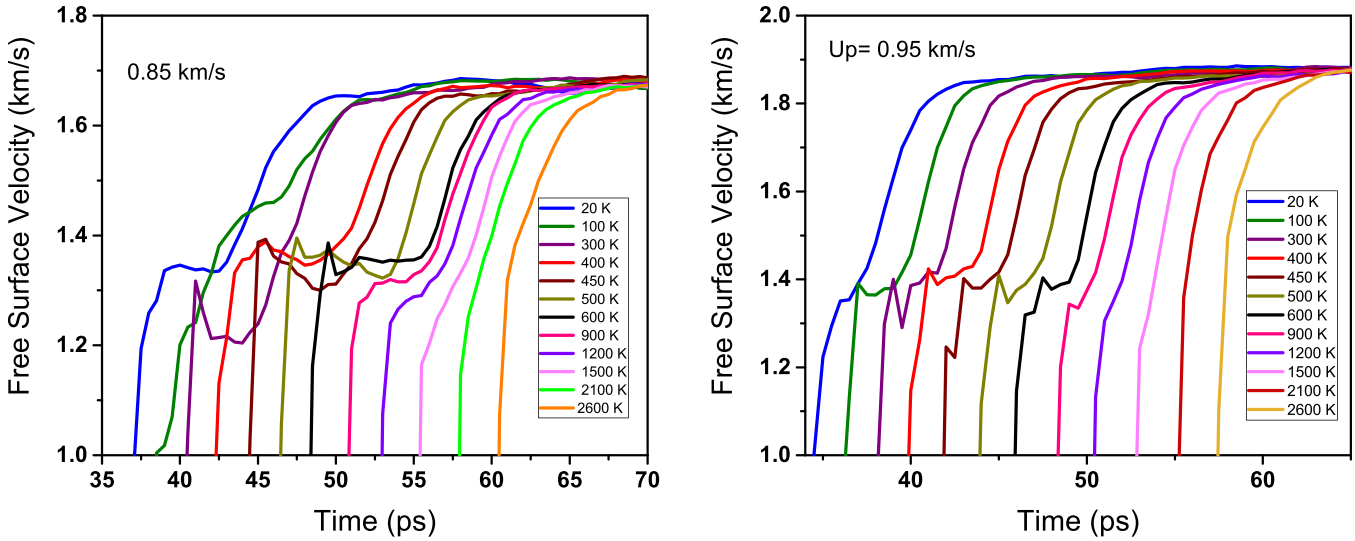

FIG. 9. FSV profile of 165-nm sample when impacted at (a) 0.85 km/s and (b) 0.95 km/s. Results for different sample temperatures are shown by different colors with an arbitrary 2 ps separation between two successive cases.

Figure 10(a) shows σ_{HEL} as a function of T for three different impact strengths. As observed for $U = 0.75$ km/s (Fig. 8), higher impacts also show maxima in dynamic strength at some characteristic temperature $T = T_c$. Moreover, the position of maximum strength shifts to the low temperature side for increasing strain rates. Thus, for $T < T_c$, the material shows a thermal hardening effect. This interesting phenomena of increasing yield strength with rise of temperature or, in other words, nonmonotonous dependence of HEL on temperature, is commonly referred to as YSA [71,72] in literature. The observed anomalous thermal behavior of yield strength for [001] single crystal Ta is the most prominent result of the present paper. Expected reduction of HEL for further increase of temperature is observed beyond this point, i.e., $T > T_c$. A closer look at Fig. 10(a) conveys that at the high-temperature regime, HEL of different impact cases merge together, indicating weak dependence of strain rate at thermally activated regions. On the contrary, for $T < T_c$, yield stress increases with strain rate. Thus, the usual constitutive laws [56,73] based on monotonically increasing/decreasing trend of flow stress with temperature cannot be applied here.

Consequently, we propose an empirical function for characterizing thermal behavior of HEL applicable in the entire regime of temperatures that predicts the observed peaking. In doing so, we hypothesize that increasing HEL at low temperature is an artifact of phonon drag. Recently, Blaschke *et al.* [74] has shown that at high strain rates, the phonon drag coefficient is directly proportional to temperature for screw dislocations, the primary mechanism of deformation for [001] bcc metals. With that background, for $T < T_c$ we express

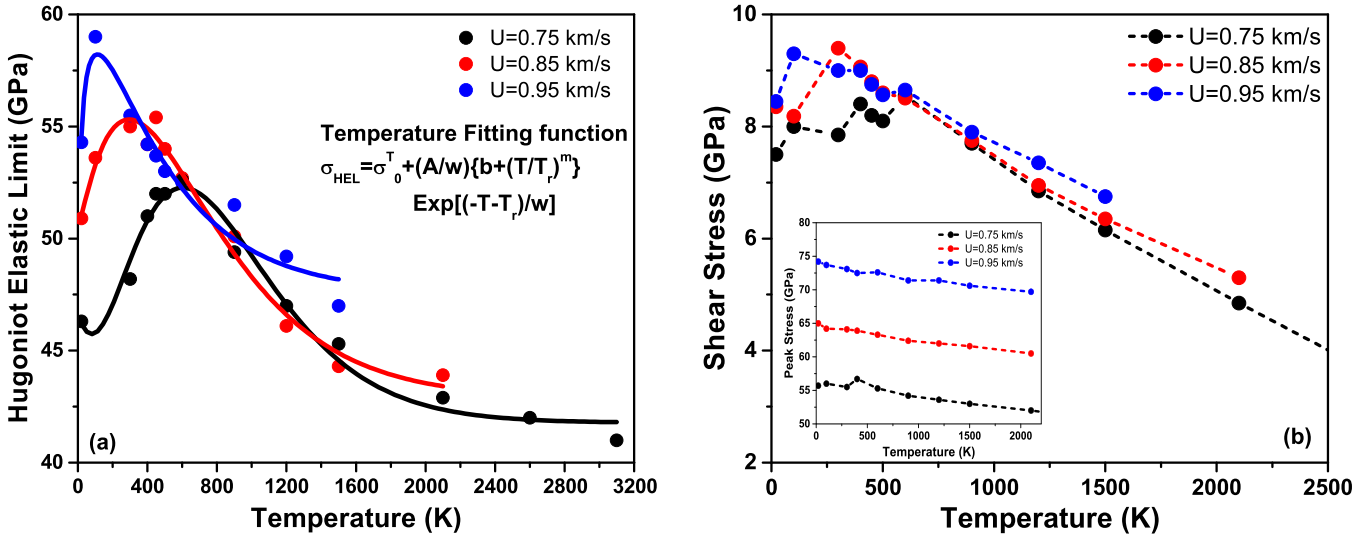

FIG. 10. Temperature variation of (a) HEL for impact velocities of 0.75 km/s (black), 0.85 km/s (red), and 0.95 km/s (blue). Symbols refer to simulation data whereas solid lines are their fits with Eq. (13). (b) Corresponding shear stress for three impact cases (symbols). Dashed lines provide guidance to eye. Inset shows the thermal influence of peak loading stress.

TABLE IV. Fitting coefficients of Eq. (13) for three different impact velocities.

U (km/s)	σ_0^T (GPa)	A (GPa/K)	w (K)	b	T_r (K)	m
0.75	41.78	2.0E4	250.6	0.21	319.6	2.5146
0.85	42.88	1.4E4	352.2	0.41	267.6	1.1406
0.95	47.59	1.0E6	402.2	−0.994	77.89	0.0018

HEL as a generalized power-law function of temperature. For $T > T_c$, it is assumed to follow exponential decay. To that end, σ_{HEL} versus T data for all strain rates are fitted with the following empirical relation:

$$\sigma_{\mathrm{HEL}} = \sigma_0^T + \frac{A}{w}\left[b + \left(\frac{T}{T_r}\right)^m\right]\exp\left[\frac{-T - T_r}{w}\right]. \quad (13)$$

Numerical values of fitting constants, A, w, b, T_r, m, σ_0^T are provided in Table IV. The extremum of this function can be obtained by making its first derivative with respect to temperature to zero. This reduces to the following equation:

$$T^m - mwT^{m-1} + bT_r^m = 0. \quad (14)$$

Solving Eq. (14) numerically, we find that maximum of σ_{HEL} occurs at $T_c = 604.6$ K, 294.6 K, and 109.5 K for $U = 0.75$, 0.85 and 0.95 km/s, respectively. The shift in T_c at higher strain rate can be observed very clearly in Fig. 10(a). Hence, characteristic temperature T_c is the one at which the power-law increase of HEL switches to exponential decay. At this critical temperature, screw and edge dislocations attain equal mobility due to thermal activation of the screw dislocations.

Physically, competitive phenomena of strain hardening and thermal activation gives rise to an observed trend around T_c. Beyond T_c, thermal activation induced softening leads to reduction of HEL, thereby making flow stress insensitive to strain rate change.

It is apparent from Fig. 10(a) that the difference between the HEL peak and its value at 20 K is about 5 GPa, which is about 10% of the 20 K estimate. Extrapolating the concepts established in Sec. VI, it can be inferred that for mm-thick targets at $\dot{\varepsilon} \approx 10^5$ s^{-1}, the difference between the HEL peak and 20 K would be negligibly small. Hence, observing such YSA will be difficult for lower strain rates. A feeble signature of YSA can be identified in experimental data of Zaretsky and Kanel [19] for 1-mm-thick samples at $\dot{\varepsilon} = 0.4 \times 10^5$ s^{-1} wherein highest HEL stress occurs for 800 K. Other experimental work on the flow stress of Ta at low to moderate strain rate showed decreasing strength with temperature [53,54,75–77].

Next, we analyze the influence of temperature on shear stress as depicted in Fig. 10(b). It is interesting to find that, like HEL, shear stress also exhibits similar peaking at same temperature, T_c. However, the peak loading stress shown in the inset of Fig. 10(b) reflects a gradual decrease with temperature.

Primarily, two governing factors play a crucial role in nucleation and multiplication of mobile dislocation that controls dynamic yield stress. They are (i) thermal fluctuation activated overcoming of obstacles on mobile dislocation paths and (ii) dislocation motion controlled by phonon drag [78]. The two mechanisms evolve differently with increasing temperature. While the thermal activation leads to a decrease of flow stress, an increase in the phonon drag coefficient with temperature supports strengthening of the material due to thermal hardening.

At high strain rates, high loading stress facilitates dislocation crossing the obstacles without thermal fluctuations. Consequently, viscous phonon drag becomes the dominant resistance of the lattice for dislocation motion. High temperature thermal hardening of a Ta single crystal is analogous to many fcc materials like Al [48,79–81], Cu [46], Ag [45]; and hcp materials like Co [82], Ti [83], where HEL stress are shown to increase even at much lower strain rates.

Single-crystal Ta beyond a certain high temperature ($T > 0.5T_M$) exhibits increased thermal fluctuation that favors overcoming obstacles and facilitates dislocation motion. This causes reduction in HEL. Thermal softening found for bcc Ta is absent in fcc or hcp materials at these strain rates.

Finally, the relative influence of strain rate and initial sample temperature on dislocation nucleation and growth, an important parameter responsible for controlling flow stress, is illustrated in the bar graph of Fig. 11. It depicts total dislocation density, individual share of screw and edge dislocation components in the range of 20 K to 2100 K. Figure 11 suggests that mechanical strength of bcc Ta is controlled

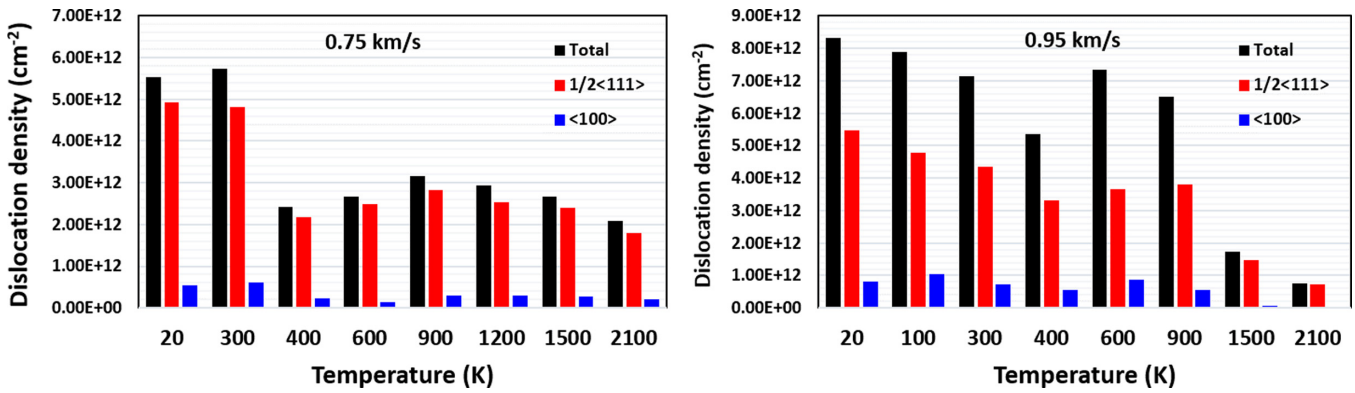

FIG. 11. Effect of temperature on generation of various types of dislocations and their densities within 165-nm target at 32 ps for two impact velocities.

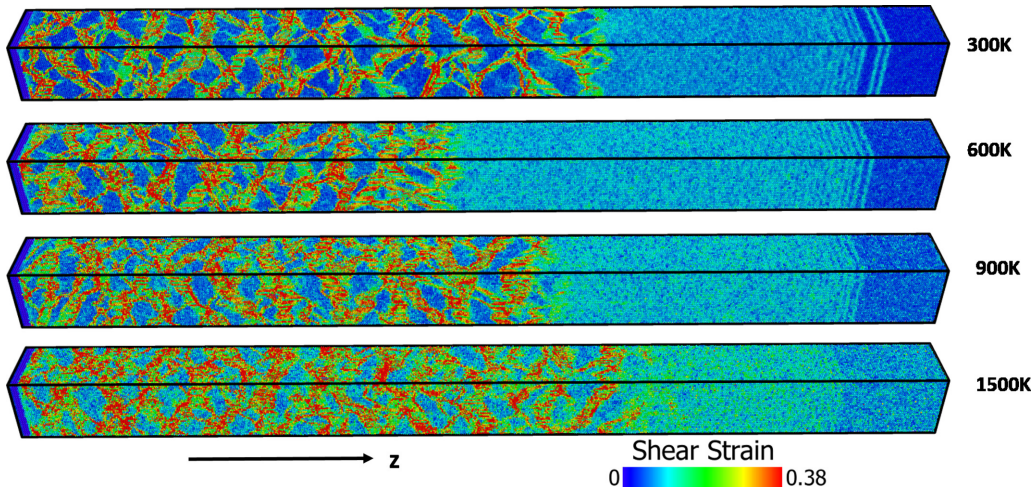

FIG. 12. Dislocation multiplication and propagation with varying sample temperatures when impacted at 0.75 km/s. Atoms have been colored according to their values of shear strain (imaging using OVITO) at 32 ps. Elastic precursors are clearly visible to arrive near free boundary. The decrease in longitudinal wave speed with increasing temperature is quite apparent. Highest strain of 0.38 is observed at 1500 K.

primarily by stress relaxation and temperature dependent mobility of screw $(1/2\langle 111\rangle$ type) dislocations.

The effect of temperature on the generation of dislocation lines and propagation of plastic waves is explained through visual plots of Fig. 12. Contour maps for different sample temperatures depict the atoms colored according to their shear strain at 32 ps. Temperature-induced decrease of longitudinal wave velocity can be clearly observed from the position of the elastic precursor front (light blue). It can be seen that at 600 K, with maximum shear strain of 0.325, dislocations have propagated shorter distance as compared to 300 K with corresponding shear strain of 0.34. Since the presence of dislocations reduces the stress required for inducing plasticity in a material, this suggests plastic transitions for 600 K at higher stress than 300 K. This could be the main reason for observed peaking at 604 K in Fig. 10(a). As temperature increases, the thermal activation leads to initial defects (clearly visible in the unshocked part of 900 K and 1500 K) and subsequent reduction in strength.

VIII. CONCLUSION

We have utilized classical MD simulations for the study of EP response of submicron (0.165-0.66 μm)-sized Ta single crystals at strain rate exceeding 10^9 s^{-1}. The study is focused on obtaining a comprehensive picture of HEL and investigation of quantitative dependence of parameters that influence HEL like sample dimension, initial temperature, peak stress, and strain rate. Important conclusions arising from our paper are summarized below.

(1) Stress-wave profile has been efficiently utilized to obtain a spatial decay law of an elastic precursor pertaining to spike and valley traits. A lateral dimension is shown to significantly influence the decay rate and hence HEL for both these features.

(2) Limitation of commonly employed FSV method in determining HEL for ultrathin samples at extremely high strain rates is discussed. Necessary modifications are suggested that resolve the inadequacy.

(3) Study of strain-rate dependence of room temperature HEL led to proposing an empirical relation. A methodology has been proposed here that utilizes the stress decay law, along with the strain-rate dependence of HEL, for predicting the strength of larger length samples with excellent accuracy. This establishes the robustness and applicability of the model for a wide range of strain rates.

(4) An empirical relation has been proposed to explain the observed YSA of thermal influence of HEL valid for such extreme strain rates. The results are explained from the evolution of dislocation density.

(5) Finally, the ideas put forward here would help in predicting HEL of larger samples using simulations in a submicron-sized one. Also, the results presented here will be useful in developing improved constitutive relations applicable for very high strain rates and temperatures.

[1] Ya. B. Zeldovich and Y. P. Raiser, *Physics of Shock Waves and High Temperature Hydrodynamic Phenomena* (Academic Press, New York, London, 1966).

[2] V. E. Fortov, Intense shock waves and extreme states of matter, Phys. Usp. **50**, 333 (2007).

[3] G. I. Kanel, V. E. Fortov, and S. V. Razorenov, Shock waves in condensed-state physics, Phys. Usp. **50**, 771 (2007).

[4] G. I. Kanel, E. B. Zaretsky, S. V. Razorenov, S. I. Ashitkov, and V. E. Fortov, Unusual plasticity and strength of metals at ultra-short load durations, Phys. Usp. **60**, 490 (2017).

[5] D. Grady, *Physics of Shock and Impact: Fundamentals and Dynamic Failure* (IOP Publishing Ltd., Bristol, UK, 2017), Vol. 1.

[6] D. Grady, *Physics of Shock and Impact: Materials and Shock Response* (IOP Publishing Ltd., Bristol, UK, 2017), Vol. 2.

[7] G. I. Kanel, On nanosecond thermophysics (Review), High Temp. **58**, 550 (2020).

[8] A. S. Khan, J. Liu, J. W. Yoon, and R. Nambori, Strain rate effect of high purity aluminum single crystals: Experiments and simulations, Int. J. Plast. **67**, 39 (2015).

[9] N. Djordjevica, R. Vignjevica, L. Kielya, S. Caseb, T. D. Vuysta, J. Campbella, and K. Hughes, Modelling of shock waves in fcc and bcc metals using a combined continuum and dislocation kinetic approach, Int. J. Plast. **105**, 211 (2018).

[10] A. Mandal and Y. M. Gupta, Elastic-plastic deformation of molybdenum single crystals shocked along [100], J. Appl. Phys. **121**, 045903 (2017).

[11] E. B. Zaretsky and G. I. Kanel, The high temperature impact response of tungsten and chromium, J. Appl. Phys. **122**, 115901 (2017).

[12] J. C. F. Millett, P. Avraam, G. Whiteman, D. J. Chapman, and S. Case, The role of orientation on the shock response of single crystal tantalum, J. Appl. Phys. **128**, 035104 (2020).

[13] E. B. Zaretsky and G. I. Kanel, Invariability of rate dependences of normalized flow stress in niobium and molybdenum under conditions of shock compression, J. Appl. Phys. **120**, 105901 (2016).

[14] A. Ray and A. Singla, Development of semiempirical equation of state of binary functionally graded materials and its influence on generation of ramp compression: Comparison with bilayer graded density impactors, Phys. Rev. B **103**, 054301 (2021).

[15] A. Ray and A. Singla, Hydrodynamic simulation of hypervelocity generation by use of functionally graded materials: Velocity enhancement study, Int. J. Imp. Engg. **152**, 103843 (2021).

[16] J. C. F. Millett, G. Whiteman, N. T. Park, S. Case, and N. K. Bourne, The role of cold work on the shock response of tantalum, J. Appl. Phys. **113**, 233502 (2013).

[17] A. Dewaele and P. Loubeyre, Mechanical properties of tantalum under high pressure, Phys. Rev. B **72**, 134106 (2005).

[18] B. Pang, S. Case, I. P. Jones, J. C. F. Millett, G. Whiteman, Y. L. Chiu, and C. A. Bronkhorst, The defect evolution in shock loaded tantalum single crystals, Acta Mater. **148**, 482 (2018).

[19] E. B. Zaretsky and G. I. Kanel, Tantalum and vanadium response to shock-wave loading at normal and elevated temperatures. Non-monotonous decay of the elastic wave in vanadium, J. Appl. Phys. **115**, 243502 (2014).

[20] J. R. Asay, T. Ao, T. J. Vogler, J. P. Davis, and G. T. Gray III, Yield strength of tantalum for shockless compression to 18 GPa, J. Appl. Phys. **106**, 073515 (2009); J. L. Ding, J. R. Asay, and T. Ao, Modeling of the elastic precursor behavior and dynamic inelasticity of tantalum under ramp wave loading to 17 GPa, *ibid.* **107**, 083508 (2010).

[21] J. R. Asay, T. J. Vogler, T. Ao, and J. L. Ding, Dynamic yielding of single crystal Ta at strain rates of $\approx 5\ 10^5\ s^{-1}$, J. Appl. Phys. **109**, 073507 (2011).

[22] S. V. Razorenov, G. I. Kanel, G. V. Garkushin, and O. N. Ignatova, Resistance to dynamic deformation and fracture of tantalum with different grain and defect structures, Phys. Solid State **54**, 790 (2012).

[23] J. L. Brown, D. P. Adams, C. S. Alexander, J. L. Wise, and M. B. Prime, Estimates of Ta strength at ultrahigh pressures and strain rates using thin-film graded-density impactors, Phys. Rev. B **99**, 214105 (2019).

[24] G. T. Gray and K. S. Vecchio, Influence of peak pressure and temperature on the structure/property response of shock-loaded Ta and Ta-10%W, Metal. Mater Trans. A **26**, 2555 (1995).

[25] S. I. Ashitkov, P. S. Komarov, E. V. Struleva, M. B. Agranat, G. I. Kanel, and K. V. Khishchenko, The behavior of tantalum under ultrashort loads induced by femtosecond laser, J. Phys: Conf. Series **653**, 012001 (2015).

[26] J. C. Crowhurst, M. R. Armstrong, S. D. Gates, J. M. Zaug, H. B. Radousky, and N. E. Teslich, Yielding of tantalum at strain rates up to $10^9\ s^{-1}$, Appl. Phys. Lett. **109**, 094102 (2016).

[27] J. H. Eggert, R. F. Smith, D. C. Swift, R. E. Rudd, D. E. Fratanduono, D. G. Braun, J. A. Hawreliak, J. M. McNaney, and G. W. Collins, Ramp compression of tantalum to 330 GPa, High Press. Res. **35**, 339 (2015).

[28] T. V. Popova, A. E. Mayer, and K. V. Khishchenko, Evolution of shock compression pulses in polymethyl methacrylate and aluminum, J. Appl. Phys. **123**, 235902 (2018).

[29] K. V. Khishchenko and A. E. Mayer, High- and low-entropy layers in solids behind shock and ramp compression waves, Int. J. Mech. Sci. **189**, 105971 (2021).

[30] R. Kositski and D. Mordehai, On the origin of the stress spike decay in the elastic precursor in shocked metals, J. Appl. Phys. **126**, 085901 (2019).

[31] J. D. Clayton and J. T. Lloyd, Analysis of nonlinear elastic aspects of precursor attenuation in shock-compressed metallic crystals, J. Phys. Commun. **2**, 045032 (2018).

[32] T. Nguyen, S. J. Fensin, and D. J. Luscher, Dynamic crystal plasticity modeling of single crystal tantalum and validation using Taylor cylinder impact tests, Int. J. Plast. **139**, 102940 (2021).

[33] L. A. Zepeda-Ruiz, A. Stukowski, T. Oppelstrup, and V. V. Bulatov, Probing the limits of metal plasticity with molecular dynamics simulations, Nature (London) **550**, 492 (2017).

[34] T. P. Remington, E. N. Hahn, S. Zhao, R. Flanagan, J. C. E. Mertens, S. Sabbaghianrad, T. G. Langdon, C. E. Wehrenberg, B. R. Maddox, D. C. Swift, B. A. Remington, N. Chawla, and M. A. Meyers, Spall strength dependence on grain size and strain rate in tantalum, Acta Mater. **158**, 313 (2018).

[35] D. Tramontina, P. Erhart, T. Germann, J. Hawreliak, A. Higginbotham, N. Park, R. Ravelo, A. Stukowski, M. Suggit, Y. Tang, J. Wark, and E. Bringa, Molecular dynamics simulations of shock-induced plasticity in tantalum, High Ener. Dens. Phys. **10**, 9 (2014).

[36] E. N. Hahn, T. C. Germann, R. Ravelo, J. E. Hammerberg, and M. A. Meyers, On the ultimate tensile strength of tantalum, Acta Mater. **126**, 313 (2017).

[37] A. Higginbotham, M. J. Suggit, E. M. Bringa, P. Erhart, J. A. Hawreliak, G. Mogni, N. Park, B. A. Remington, and J. S. Wark, Molecular dynamics simulations of shock-induced deformation twinning of a body-centered-cubic metal, Phys. Rev.B **88**, 104105 (2013).

[38] E. Etemadi, J. Zamani, and M. Jafarzadeh, Physical constitutive equations for plastic deformation of fcc metals subjected to high strain rate loading, Proc. IMechE Part L: J. Materials: Design and Appl. **232**, 106 (2018).

[39] R. A. Austin and D. L. McDowell, A dislocation-based constitutive model for viscoplastic deformation of fcc metals at very high strain rates, Int. J. Plast. **27**, 1 (2011).

[40] L. Koci, E. M. Bringa, D. S. Ivanov, J. Hawreliak, J. McNaney, A. Higginbotham, L. V. Zhigilei, A. B. Belonoshko, B. A. Remington, and R. Ahuja, Simulation of shock-induced melting of Ni using molecular dynamics coupled to a two-temperature model, Phys. Rev. B **74**, 012101 (2006).

[41] G. Mogni, A. Higginbotham, K. Gaal Nagy, N. Park, and J. S. Wark, Molecular dynamics simulations of shock-compressed single-crystal silicon, Phys. Rev. B **89**, 064104 (2014).

[42] T. R. Mattsson, J. Matthew D. Lane, K. R. Cochrane, M. P. Desjarlais, A. P. Thompson, F. Pierce, and Gary S. Grest, First-principles and classical molecular dynamics simulation of shocked polymers, Phys. Rev. B **81**, 054103 (2010).

[43] S. L. Chaplot and S. K. Sikka, Molecular-dynamics simulation of shock-stress-induced amorphization of α-quartz, Phys. Rev. B **61**, 11205 (2000).

[44] R. Ravelo, T. C. Germann, O. Guerrero, Q. An, and B. L. Holian, Shock-induced plasticity in tantalum single crystals: Interatomic potentials and large-scale molecular-dynamics simulations, Phys. Rev. B **88**, 134101 (2013).

[45] E. B. Zaretsky and G. I. Kanel, Plastic flow in shock-loaded silver at strain rates from 10^4 s^{-1} to 10^7 s^{-1} and temperatures from 296 K to 1233 K, J. Appl. Phys. **110**, 073502 (2011).

[46] E. B. Zaretsky and G. I. Kanel, Response of copper to shock-wave loading at temperatures up to the melting point, J. Appl. Phys. **114**, 083511 (2013).

[47] B. Gurrutxaga-Lerma, M. A. Shehadeh, D. S. Balint, D. Dini, L. Chen, and D. E. Eakins, The effect of temperature on the elastic precursor decay in shock loaded fcc aluminium and bcc iron, Int. J. Plast. **96**, 135 (2017).

[48] E. B. Zaretsky and G. I. Kanel, Effect of temperature, strain, and strain rate on the flow stress of aluminum under shock-wave compression, J. Appl. Phys. **112**, 073504 (2012).

[49] R. A. Austin, Elastic precursor wave decay in shock compressed aluminum over a wide range of temperature, J. Appl. Phys. **123**, 035103 (2018).

[50] E. B. Zaretsky, Impact response of titanium from the ambient temperature to 1000 °C, J. Appl. Phys. **104**, 123505 (2008).

[51] G. I. Kanel, G. V. Garkushin, A. S. Savinykh, S. V. Razorenov, T. de Resseguier, W. G. Proud, and M. R. Tyutin, Shock response of magnesium single crystals at normal and elevated temperatures, J. Appl. Phys. **116**, 143504 (2014).

[52] T. de Resseguier, E. Lescoute, and D. Loison, Influence of elevated temperature on the wave propagation and spallation in laser shock-loaded iron, Phys. Rev. B **86**, 214102 (2012).

[53] K. G. Hoge and A. K. Mukherjee, The temperature and strain rate dependence of the flow stress of tantalum, J. Mat. Sci. **12**, 1666 (1977).

[54] G. P. Skoro, J. R. J. Bennett, T. R. Edgecock, and C. N. Booth, Yield strength of molybdenum, tantalum and tungsten at high strain rates and very high temperatures, J. Nucl. Mat. **426**, 45 (2012).

[55] G. V. Garkushin, A. S. Savinykh, S. V. Razorenov, and G. I. Kanel, Influence of high-temperature annealing on the resistance to high strain rate and fracture of tantalum at temperatures of 20 and 500 °C, Tech. Phys. **64**, 674 (2019).

[56] F. J. Zerilli and R. W. Armstrong, Description of tantalum deformation behavior by dislocation mechanics based constitutive relations, J. Appl. Phys. **68**, 1580 (1990).

[57] S. Plimpton, Fast parallel algorithms for short-range molecular dynamics, J. Comput. Phys. **117**, 1 (1995).

[58] W. Li, E. N. Hahn, X. Yao, T. C. Germann, and X. Zhang, Shock induced damage and fracture in SiC at elevated temperature and high strain rate, Acta Mater. **167**, 51 (2019).

[59] A. K. Subramaniyan and C. T. Sun, Continuum interpretation of virial stress in molecular simulations, Int. J. Solids Struc. **45**, 4340 (2008).

[60] A. Stukowski, Visualization and analysis of atomistic simulation data with OVITO-the Open Visualization Tool, Modelling Simul. Mater. Sci. Eng. **18**, 015012 (2010).

[61] O. Torrents Abad, J. M. Wheeler, J. Michler, A. S. Schneider, and E. Arzt, Temperature-dependent size effects on the strength of Ta and W micropillars, Acta Mater. **103**, 483 (2016).

[62] A. S. Schneider, D. Kaufmann, B. G. Clark, C. P. Frick, P. A. Gruber, R. Mönig, O. Kraft, and E. Arzt, Correlation Between Critical Temperature and Strength of Small-Scale bcc Pillars, Phys. Rev. Lett. **103**, 105501 (2009).

[63] D. Kaufmann, R. Mönig, C. A. Volkert, and O. Kraft, Size dependent mechanical behaviour of tantalum, Int. J. Plast. **27**, 470 (2011).

[64] E. N. Hahn, T. C. Germann, R. J. Ravelo, J. E. Hammerberg, and M. A. Meyers, Non-Equilibrium molecular dynamics simulations of spall in single crystal tantalum, AIP Conf. Proc. **1793**, 070006 (2017).

[65] J. W. Swegle and D. E. Grady, Shock viscosity and the prediction of shock wave rise times, J. Appl. Phys. **58**, 692 (1985).

[66] D. E. Grady, Structured shock waves and the fourth power law, J. Appl. Phys. **107**, 013506 (2010).

[67] R. Kositski and D. Mordehai, A dislocation-based dynamic strength model for tantalum across a large range of strain rates, J. Appl. Phys. **129**, 165108 (2021).

[68] C. S. Deo, D. J. Srolovitza, W. Caic, and V. V. Bulatov, Stochastic simulation of dislocation glide in tantalum and Ta-based alloys, J. Mechanics Phys. Solids. **53**, 1223 (2005).

[69] M. D. Furnish, W. D. Reinhart, W. M. Trott, L. C. Chhabildas, and T. J. Vogler, Variability in dynamic properties of tantalum: Spall, hugoniot elastic limit and attenuation, in *Proceedings of the Conference of the American Physical Society Topical Group on Shock Compression of Condensed Matter*, edited by M. D. Furnish, M. Elert, T. P. Russell, and C. T. White, AIP Conference Proc. No. 845 (AIP, New York, 2006), p. 615.

[70] D. Errandonea, B. Schwager, R. Ditz, C. Gessmann, R. Boehler, and M. Ross, Systematics of transition-metal melting, Phy. Rev. B **63**, 132104 (2001).

[71] D. Caillard, Yield-stress anomalies and high temperature mechanical properties of intermetallics and disordered alloys, Mat. Sci. Engg A **319**, 74 (2001).

[72] S. Gupta and C. A. Bronkhorst, Crystal plasticity model for single crystal Ni-based superalloys: Capturing orientation and temperature dependence of flow stress, Int. J. Plast. **137**, 102896 (2021).

[73] D. J. Steinberg, S. G. Cochran, and M. W. Guinan, A constitutive model for metals applicable at high strain rate, J. Appl. Phys. **51**, 1498 (1980).

[74] D. N. Blaschke, E. Mottola, and D. L. Preston, Dislocation drag from phonon wind in an isotropic crystal at large velocities, Phil. Mag. **100**, 571 (2020).

[75] M. Yaghoobi and G. Z. Voyiadjis, The effects of temperature and strain rate in fcc and bcc metals during extreme deformation rates, Acta Mater. **151**, 1 (2018).

[76] D. H. Lassila, A. Goldberg, and R. Beckerm, The effect of grain boundaries on the athermal stress of tantalum and tantalum-tungsten alloys, Metall. Mater. Trans. A **33**, 3457 (2002).

[77] N. R. Barton, J. V. Bernier, R. Becker, A. Arsenlis, R. Cavallo, J. Marian, M. Rhee, H.-S. Park, B. A. Remington, and R. T. Olson, A multiscale strength model for extreme loading conditions, J. Appl. Phys. **109**, 073501 (2011).

[78] A. Yu. Kuksin and A. V. Yanilkin, Atomistic simulation of the motion of dislocations in metals under phonon drag conditions, Phys. Solid State **55**, 1010 (2013).

[79] G. I. Kanel, S. V. Razorenov, K. Baumung, and J. Singer, Dynamic yield and tensile strength of aluminum single crystals at temperatures up to the melting point, J. Appl. Phys. **90**, 136 (2001).

[80] B. Zuanetti, S. D. McGrane, C. A. Bolme, and V. Prakash, Measurement of elastic precursor decay in pre-heated aluminum films under ultra-fast laser generated shocks, J. Appl. Phys. **123**, 195104 (2018).

[81] V. Garkushin, S. V. Razorenov, and G. I. Kanel, Resistance to deformation and fracture of aluminum AD1 under shock-wave loading at temperatures of 20 and 600 C, Phys. Solid State **52**, 2369 (2010).

[82] E. B. Zaretsky, Impact response of cobalt over the 300-1400 K temperature range, J. Appl. Phys. **108**, 083525 (2010).

[83] G. I. Kanel, S. V. Razorenov, E. B. Zaretsky, B. Herrman, and L. Meyer, Thermal softening and hardening of titanium and its alloy at high strain rates of shock-wave deforming, Phys. Solid. State. **45**, 656 (2003).